AN ABSTRACT OF THE THESIS OF

Joseph M. Skitka for the degree of Master of Science in Mechanical Engineering presented on June 17, 2013.

Title: Development of a Cartesian-Grid-Based Solver for an Oscillatory Boundary Layer over a Rough Wall

Abstract approved: _____

Sourabh V. Apte

Predominant models for predicting rates of sediment transport face acute shortcomings when applied to coastal boundary layers [58]. This is due to a neglect of the web of stochastic variables governing the rate of sediment dislodgement. While stochastic models do exist, the parametric extent of their validity tends to be limited, and none have taken into account an understanding of phase dependence in application to oscillatory flow, likely because the existing knowledge of the evolution of flow properties throughout a cycle of wave motion is insubstantial. A detailed understanding of the statistical properties of sediment forces and motion is a precondition to the development of specific models for oscillatory flows. Experiments on such flows tend to be limited by the small length and time scales of the particles. Numerical simulations offer flexibility in measuring many properties simultaneously in hard-to-reach places without disturbing the delicate dynamics of particle ejection. Fully resolved simulations of purely oscillatory flow over an idealized sediment geometry were performed at moderate parameter ranges near the transition to turbulence. Due to the computational challenges posed by this flow type, a new structured, fully parallelized, incompressible-flow, finite-volume solver along with effective and generalized immersed-boundary tools was developed and validated against benchmark simulations.

Turbulence statistics and their correlation with the statistics of forces on the sediment bed are analyzed. Large divergences from Gaussian behavior are found in the bed velocity during accelerating phases of the cycle, and the probability distribution functions of fluctuations in the bed-flow velocity, u_b^2, and lift appear to follow this trend. The results suggest that coherent structures thought to be linked to sediment ejection in laminar flow regimes have a diminished effect on particle forces in transitional and early turbulent regimes. The implications of these findings on model development will be discussed.

Development of a Cartesian-Grid-Based Solver for an Oscillatory Boundary Layer over a Rough Wall

by

Joseph M. Skitka

A THESIS

submitted to

Oregon State University

in partial fulfillment of
the requirements for the
degree of

Master of Science

Presented June 17, 2013
Commencement June 2014

Master of Science thesis of Joseph M. Skitka presented on June 17, 2013.

APPROVED:

_____

Major Professor, representing Mechanical Engineering

_____

Head of the Department of the School of Mechanical, Industrial, and Manufacturing Engineering

_____

Dean of the Graduate School

I understand that my thesis will become part of the permanent collection of Oregon State University libraries. My signature below authorizes release of my thesis to any reader upon request.

_____

Joseph M. Skitka, Author

ACKNOWLEDGEMENTS

TABLE OF CONTENTS

LIST OF FIGURES

LIST OF FIGURES (Continued)

LIST OF FIGURES (Continued)

LIST OF TABLES

Chapter 1   Introduction

Near-shore sediment transport on a large scale, considered the domain of coastal morphodynamics and coastal engineering, is responsible for shoreline erosion, and, on an even longer scale, the geomorphological evolution of coasts. Modeling these phenomena implies the challenge of resolving disparate scales. Solutions of interest exist on the order of years and decades (or even much longer) yet are ultimately governed by hydrodynamic mechanisms of particle motion, often enduring for only a fraction of a second. The importance of an accurate understanding of these mechanisms to large-scale models has been recognized [45], and, as a result, the issue has been garnering attention in fields related to hydrodynamics.

Many hydrodynamic investigations of oscillatory flows over sediment have focused on general characterization of the flows rather than developing specific insight for transport models. Experimental studies of an oscillating rough bed in stationary flow were conducted by Keiller and Sleath (1975) [30] at laminar parameter ranges. They compared flows over sediment particles to idealized Stokes flows over flat plates and found velocity profiles featured multiple local maxima per cycle above the spheres. Sleath (1986) [51] investigated turbulent parameter ranges more likely to cause sediment motion. Recent simulations have provided more details on these flows. Fornarelli and Vittori (2009) [22] observed large horseshoe-shaped vortices in laminar parameter ranges which were ejected from behind the sediment particles at every half cycle, explaining the additional velocity peaks in Keiller and Sleath (1975) [30]. Ding and Zhang [16] simulated oscillatory flows over multiple sediment packing configurations in order to verify basic flow properties.

At the same time the study of small-scale fluid-sediment interaction as applied to steady flows has been underway for decades. From this perspective, sediment motion is broken up into incipient motion, transport, and deposition. These events describe motion in both the bed load and suspended load. Bed load is comprised of sediment which is in motion but supported by the sediment bed; its motions are due to sliding and rolling. The suspended load is comprised of sediment particles which are typically smaller than those in the bed load and are supported by the fluid.

Rates of incipient motion have historically been modeled using single-parameter techniques. Shields (1936) was the first to do this, proposing the relative strength of the bed shear stress to the gravitational force on the particles as a useful parameterization, $\theta = \frac{\tau_w}{(\rho_{sed} - \rho_{fl})gD}$ [46]. The rates of pickup and, therefore, the supported bed load and sediment flux are commonly modeled as a linear

function of the Shields parameter $\theta - \theta_c$, where θ_c is the critical Shields parameter, an empirically determined value indicating the onset of motion. More recently, Sleath has proposed an analogous single-parameter model for rates of sediment motion in oscillatory flow by replacing the bed shear stress with the oscillating pressure gradient, $S = \frac{\rho_{fl} U_\infty \omega}{(\rho_{sed} - \rho_{fl}) g}$, termed the Sleath parameter [53]. At smaller values of S ($\lesssim 0.1$) the Shields parameter is still sufficient to characterize the flows, even if oscillatory, while for larger values, both parameters need to be considered [40].

More accurate, stochastic techniques have also been in development for steady flows for some time [18]; typically, a probability distribution function of turbulent fluctuations is assumed in a specific flow variable (such as a Gaussian velocity distribution), which is then related analytically to the forces experienced by the particles [11, 15, 26, 41, 58], while more recently, log-normal distributions have been assumed in the turbulent intensities [7, 10, 12, 57]. Despite having substantial predictive potentials, these methods have not been incorporated in a generalized stochastic model of oscillatory flows. A promising approach to shedding light on the small-scale hydrodynamics involved in coastal processes is the characterization of the effects of punctuated turbulent events on sediment pickup and transport while simultaneously developing stochastic models for the oscillatory case.

The simulation of highly resolved moving sediment in oscillatory flows could be of particular benefit to advancing the understanding of transport mechanisms and models. Fully resolved particle-laden flows, such as those of Chan-Braun et al. (2011) [8] have directly provided details of particle densities and rates of suspension and transport in steady flows, yet such simulations have not been performed for oscillatory flows.

These simulations are particularly challenging from a computational perspective. Statistics regarding particle positions and motions require large numbers of particles, which simultaneously need to be fully-resolved to accurately reflect the small-scale hydrodynamics affecting their behavior. In addition, the oscillatory spatial displacement of fluid is vast (meters) compared to typical sediment particle sizes (sub-millimeter), resulting in the need for large fluid domains to attempt to resolve both of these scales completely. Solvers which treat both fluid and particle motion in a highly efficient manner are needed to simulate such flows effectively.

It is the intention of this project to develop a solver suitable for use with the challenging simulations of fully-resolved particle-laden oscillatory flows and to use this solver to understand stochastic flow and particle properties and their potential use in coastal sediment transport models.

Chapter 2   Background

2.1   Models of Sediment Motion

Analytical models of sediment transport date back to Shields (1936) [46], which defined a non-dimensional parameter relating gravitational forces to the dynamic pressure written in terms of the wall shear stress, τ_w. This has become known as Shields parameter and is defined as $\theta \equiv \frac{\tau_w}{(\rho_{sed} - \rho_{fl})gD}$, where ρ_{sed} and ρ_{fl} are the particle and fluid densities respectively, g is the acceleration of gravity on earth, and D is the average particle diameter. Critical values of the Shields parameter, θ_c, at which the onset of sediment motion occurs, are found empirically and used to predict rates of sediment-load movement with a simple linear relationship ($\propto \theta - \theta_c$). According to Nichols and Foster (2009), typical critical Shields parameters for steady flow are $\theta_c \approx 0.05$, with different transport regimes occurring as the Shields parameter increases [40]. Various adaptations on this model exist, incorporating additional parameters like sediment shape and exposure or devising a non-linear dependence on $\theta - \theta_c$ [23] [58], and have been widely used in the decades since to describe sediment pick-up probabilities in steady flows.

Many of these deterministic models face limitations at extreme parameter ranges, both at high relative shear stress and long time scales with bed shear stress below the critical value, where the linear models and adaptations unphysically experience a discontinuity in the first derivative when going to zero. More accurate descriptions can be developed by solving for the probability of particle entrainment based on stochastic flow properties. Such a probability can be determined by integrating the probability distribution functions (PDFs) of lift, drag, or shear stress acting on particles over the range of forces which would result in sediment dislodgment, that is $F > F_{c,1}$ or $F < F_{c,2}$ where F is the force in question (e.g. lift) and $F_{c,1}$ and $F_{c,2}$ are critical values of forces at which motion occurs [41] [7]:

$$P = 1 - \int_{-F_{c,1}}^{F_{c,2}} \mathrm{PDF}(F) dF, \tag{2.1}$$

where P is the probability of dislodgement. Sediment loads can then be solved for by balancing this rate of pickup with the rate of deposition, which is also a function of the sediment load. Such models are more readily customized to incorporate multiple probabilistic parameters by combining or transforming PDFs.

Stochastic models began with the early work of Einstein (1950) [18], which was novel for presenting a separate probabilistic treatment of bed-load transport for sediment grain dragging and rolling on the alluvial bed, distinct from the strictly suspended sediment load. This formulation was based on the assumption of the PDF of the bed-pressure fluctuations being Gaussian. While this bed-load function was still a considerable simplification of the physical phenomena involved, it avoided unphysical cutoffs of the transport function by not requiring the forces acting on the particle to lift it off of the bed.

More recently, theoretical derivations have been used to produce the PDFs of lift and drag from flow parameters. These derivations often start with an assumption about the statistics of the flow parameters. Most commonly, a Gaussian distribution is assumed for the PDF of the bed velocity, u_b, which is the velocity immediately above the bed surface in the log layer. Given that pressure forces play a dominant role in initiating particle motion, which is true of parameter ranges of interest for sediment transport in open-channel steady flows [15] and from oscillatory flows [22], forces on sediment are commonly related to the dynamic pressure via

$$F_L = \frac{1}{2}C_L \rho_{fl} u_b^2 A \tag{2.2}$$

$$F_D = \frac{1}{2}C_D \rho_{fl} u_b^2 A \ , \tag{2.3}$$

where F_L and F_D are the lift and drag experienced by the sediment particle, C_L and C_D are the lift and drag coefficients, ρ_{fl} is the fluid density, and A is the cross-sectional area of the particle. The pressure dominance is expected to vary in the case of the drag component depending flow parameters and geometry; for instance Ma and Williams (2009) noted that viscous forces have a sizable impact on the streamwise moment of rotation in steady flow over a hexagonal sphere packing at $Re_\tau = \frac{u_\tau D}{\nu} = 533$, where u_τ is the wall velocity, D is the particle diameter, and ν is the kinematic viscosity [34]. Most statistical derivations of forces on the particles do not attempt to explicitly justify the use of these relations. Papanicolaou et al. (2002) used a Gaussian assumption of the bed velocity to derive a χ^2-distribution for u_b^2, which is used to derive distributions for sediment drag and lift on embedded particles (see figure 2.1 for PDF comparison). Exposed spheres were then modeled with the vertical component of velocity intensity w_b^2, an unusual approach.

Regarding the assumption of Gaussian velocity profiles, note that exactly Gaussian velocity fluctuation profiles are rather unusual outside of isotropic flow. Turbulent shear flows, being anisotropic, are characterized by nonuniform regions of turbulent kinetic energy production. The turbulent energy cascade then favors the transport of energy from regions of high TKE production to randomly distributed patches of high dissipation, resulting in distributions of turbulent flow properties which
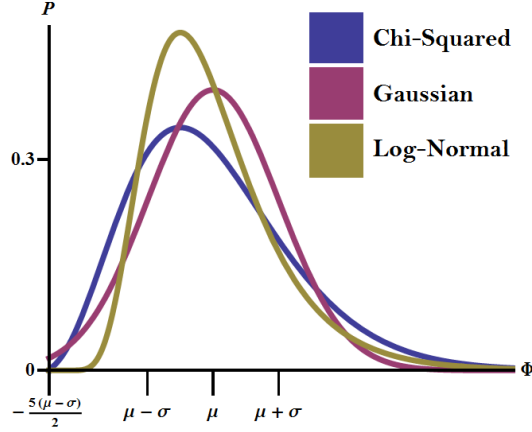
Figure 2.1: Gaussian, log-normal, and χ^2 distributions centered 2.5 standard deviations positive of zero for some variable Φ, where μ is the mean and σ is the standard deviations. The probability is consistent with Φ being normalized by σ. Note that the Gaussian predicts a much more rapid decline of the positive-tail values.

are skewed and peaked (high kurtosis) [55]. Applying this reasoning to the case of oscillatory flow, one might hypothesize that TKE is being generated primarily due to the instabilities in the regions of high velocity gradients around the fluid-particle interface near the peak velocities of the cycle, so the assumption of a Gaussian profile is expected to apply poorly. It may also be hypothesized that TKE dissipation should be non-local and that phases characterized by large TKE dissipation may feature symmetric velocity distributions.

Hofland et al. (2006) repeats the χ^2 derivation for the special case of $D \propto u_b \, |u_b|$, which allows for the drag to be negative when velocity reverses direction [26]. This only becomes relevant at high relative turbulence intensities, $r_u = \frac{\sigma_{u_b}}{\bar{u}_b}$, where σ_{u_b} is the standard deviation of u_b and $\bar{u}_b$ is, for the case of steady flows, the time averaged bed velocity. The resulting PDFs are written as a function of the relative turbulence intensity. The model fit data very well from open-channel flows but did not reproduce the statistics in the wake of a backward facing step. Based on the results of this study, as well as those from Hofland's PhD thesis [25], these models appear to work poorly, either getting the central profile correct while failing at the tails of the distribution, or vice versa. Detert et al. (2010), for instance, tested the modified χ^2-functions of Hofland et al. (2006) against experimental data revealing shortcomings in their fit of lift and drag PDFs in open channel flows, particularly at the tails of the distributions [15]. Prooijen and Winterwerp (2010) attempted to use this model to fit empirical data; however, in achieving this fit, they manipulate the distribution without offering any physical motivation for this change other than its convenience.

An increasingly common assumption for derivations of PDFs of the sediment forces is that u_b^2 or τ_w are described by log-normal distributions (see figure 2.1 for PDF comparison). One of the earlier publications of note on this topic is Cheng and Law (2003) [12], which has been frequently referred to by subsequent studies. Like the use of the Gaussian distribution, the log-normal was given no physical justification by it's users other than that it has the desirable properties of being positively skewed and is always positive. However, the report of Mouri et al. (2009) [39] has recently addressed this assumption with refreshing physical clarity. This article featured rigorous experiments on isotropic turbulence, jet flows, and boundary-layer flows to determine the universality of the fluctuations of turbulent properties. A log-normal distribution was found to describe the distributions of turbulent dissipation and intensities with consistent standard deviations between all three flow types at a given Reynolds number. The log-normal distribution is interpreted as the result of the central limit theorem applied to the logarithm of the product of a large number of slightly correlated random variables. The correlation between these variables, observed as the temporal synchronization of turbulence at different scales, is manifested through a multiplicative process. The natural logarithm of such a product can be decomposed into a summation of the logarithms of the constituent variables representing a massive number of interactions across different scales of turbulence. The statistics of the logarithms themselves behave as independent random variables. Given this, the PDF of their sum will be a Gaussian by a generalized central limit theorem. Such a Gaussian, their reasoning goes, is the logarithm of the PDF of the intensity and dissipation. It should be noted that this does not preclude the possibility of normally distributed constituent variables and so, if correct, would not invalidate Gaussian velocity assumptions, but speculation as to the specific statistical mechanics which result in such a system of variables is not offered. Flows conditions suitable for log-normal modeling are described as being $1 < \frac{r}{L_u} < 100$, where r is the length scale of turbulence in question and L_c is the correlation length. At smaller scales, the turbulence is expected to become completely uncorrelated, and the interactions of turbulent intensities and dissipation become additive thereby producing a Gaussian distribution of intensity and dissipation by the central limit theorem.

The work of Cheng (2006) is worth noting because of its inclusion of a Gaussian PDF for particle size distributions, which was transformed by means of the inverse relationship, $\tau_b \propto \frac{1}{D}$, into a contribution to the PDF of bed shear stress, τ_b [10]. This was artfully approximated as a log-normal relationship, allowing for the combination of these separate effects into a single expression for the PDF and highlighting the inherent advantage of the log-normal distribution in that multiplicative processes of a compatible form combine easily.

Celik et al. (2010) used the log-normal distribution to describe their models of impulse on a free, exposed sphere atop a regular sediment packing in steady channel flows [7]. Valyrakis et al.

(2011) acknowledge the merits of the log-normal distribution proposed by that experiment, which was motivated in part by [39], yet points out that unlikely, extreme force fluctuations are not accurately predicted by this distribution [57] . It has been noted that the log-normal distribution may not apply to very unlikely values [39]; however, it is possible that the experiments of [7] were not characterized by the correct length scales for the log-normal fluctuations to apply.

It has been observed that sediment grains act as low-pass filters, removing the force of high-wavenumber fluctuations through surface averaging [26], so it is possible that particles will respond to a sufficiently specific spatial range of turbulent fluctuations to experience a behavioral regime featuring dominance of log-normal fluctuations. Based on the physical explanation of Mouri et al. (2009), it can be expected that sediment realistically and frequently experience Gaussian fluctuations of forces in the case of larger length scales.

In the case of embedded particle motion, ejection is primarily caused by lift forces as opposed to drag forces due to horizontal constraints on motion by neighboring particles, so an awareness of the mechanisms responsible for generating lift on these particles in specific flow types is necessary for understanding the onset of particle motion. As mentioned previously, at Shields parameters nearing θ_c, only the most unlikely and energetic fluctuations in lift will be capable of particle dislodgment. A detailed knowledge of the probability distribution function (PDF) of the lift in terms of the general flow parameters would give a complete description of the occurrence of initial motion and good indication of the likelihood of complete ejection. Other factors influencing ejection are the change in lift forces as a particle is displaced as well as the temporal autocorrelation of the lift; sufficient energy is required to overcome the potential well of the particle's resting position which must be provided by lift forces of sufficient magnitude persisting over a period of time [17]. In the case of exposed particles, the introduction of a gap beneath a particle can introduce fast moving fluid which contributes to restoring the particle via pressure forces [20], but the effect of a gap is expected be different in the case of an embedded particle.

2.2   Oscillatory Flows

While oscillatory flow over a sediment bed has several degrees of freedom, oscillatory flow over a flat wall has only one, which is typically represented by $Re_\delta = \frac{U_\infty \delta}{\nu}$, where $\delta = \sqrt{\frac{2\nu}{\omega}}$ is the Stoke's-layer thickness, U_∞ is the maximum velocity achieved by the fluid far from the wall every cycle, ω is the frequency of oscillations in radians, and ν is the kinematic viscosity [60]. The choice of this parameter follows from its prominence in the analytical solution to this flow (at sufficiently low Reynolds numbers) [54]

$$u(z,t) = U_\infty \left(Cos\left(\omega t\right) - e^{\sqrt{\frac{\omega}{2\nu}}z} Cos\left(\omega t - \sqrt{\frac{\omega}{2\nu}}z\right)\right), \qquad (2.4)$$

where U_∞ is the maximum velocity far from the wall:

$$u_\infty(\phi) = u(z \to \infty) = U_\infty Sin\left(\omega t\right), \qquad (2.5)$$

where $\phi = \omega t$ is the phase of the cycle in radians. For the sake of clarity, the time-dependent variable $u_\infty(\phi)$ will, like all temporally or spatially varying quantities in this thesis, be lower case and will always reference (ϕ), while the general flow parameter U_∞ will always be capitalized.

A second degree of freedom in the sediment case is introduced by the relative length scales of the turbulence and sediment elements and, in this report, is given the straightforward representation of $\frac{D}{\delta}$, where D is the sphere diameter.

$$\text{Flow Parameters:} \qquad Re_\delta = \frac{U_\infty \delta}{\nu} \qquad ; \qquad \frac{D}{\delta} \qquad (2.6)$$

Alternative sets of parameters are formed out of combinations of $Re_a = \frac{aU_\infty}{\nu} = 2Re_\delta^2$, where a is the amplitude of spatial oscillations far from the wall [22] [16] [51], $Re_D = \frac{DU_\infty}{\nu}$ (common in oscillatory flow over a single sphere [20]), and the Keulegan-Carpenter number, $\tau = \frac{TU}{D}$, where $T = \frac{2\pi}{\omega}$ is the period of oscillation [20], which is the relative magnitude of the period with respect to the time it takes flow to move past a particle. Keiller and Sleath (1975) use $\frac{U_\infty}{\omega D} = Re_\delta * \frac{\delta}{2D}$ [30]. For the purposes of this thesis, $\{Re_\delta, \frac{D}{\delta}\}$ will be used to ease comparison with oscillatory flows over flat surfaces.

Another degree of freedom is introduced by the weight of the particles when they are free to move. Analogous to the Shields parameter, Sleath proposed the relative force of oscillatory pressure gradient driving the wave motion to that of gravity, $S = \frac{\rho_{fl}U_\infty\omega}{(\rho_{sed}-\rho_{fl})g}$, now called the Sleath parameter, for parameterization of sediment motion in oscillatory coastal environments [53]. It was originally determined that the Shields parameterization would be sufficient for accurate flow modeling at Sleath parameters $S \quad 0.3$, while the Sleath parameter was accurate for $S \gtrsim 0.3$; however, Nichols and Foster (2009) found that both parameters were important at ranges down to $S = 0.1$ [40]. Together, the Shields and Sleath parameters can be thought of as comprising a single degree of freedom.

As seen in equation 2.4, in oscillatory flow over a flat wall, wall disturbances induced on the far-field flow decay exponentially with increasing height with a decay constant δ. These disturbances, manifested as both amplitude damping and phase lag, are characterized by staggered regions of op-

positely vorticity which gradually decay with height [13]. Vittori and Verzicco (1998) found via fully resolved simulations that, given small surface imperfections, flows of $Re_\delta < 100$ are laminar, those of $100 < Re_\delta$ 550 are in a disturbed laminar regime, and those of $Re_\delta \gtrsim 550$ are fully turbulent [60], while Jensen et al (1988) described a hazier transition region ranging from 200 Re_δ 900 based on their experiments over a smooth surface [28].

Flow over a plate oscillating in a plane in steady fluid is of historical significance. This has an analytical solution of

$$u^*(z,t) = U_\infty e^{\sqrt{\frac{\omega}{2\nu}}z} Cos \quad \omega t - \quad \overline{\frac{\omega}{2\nu}} z \tag{2.7}$$

[54] and is distinct from equation 2.4 only through the imposition of a temporally sinusoidal pressure gradient, the oscillatory solution of which can be added linearly to the moving-fluid version. This is of relevance because the most prominent experimental studies of oscillatory flow over sediment have been conducted in this altered frame of reference in which the bed is oscillating and the fluid is stationary; this will be referred to as the fluid-frame for the duration of this paper, and when appropriate, the oscillating-fluid case will be distinguished as the sediment frame through the use of $*$, as in u^*. These two frames can be considered physically interchangeable for flat plates and interchangeable to an approximation for three-dimensional flows; however, Krstic and Fernando (2001) have raised concerns that the boundary conditions appropriate for making this comparison would not have been possible to enforce in common experimental setups, such as that of Keiller and Sleath (1975) [30], calling into question the results of this study [32]. These will nonetheless be used for comparison for the early stages of the present study as they are a frequent object of comparison for simulations of these flows; substantial error should have already been recognized, and if inaccuracies do exist in these experiments, it would be of benefit to find them.

Laminar oscillatory flow cases which include a sediment bed feature a phase lag and amplitude damping similar to that of a smooth bed in the near wall region. The porosity of the sediment results in an effective bed location which is somewhere between the sediment crests and the base wall. This can be approximated by extrapolating phase-lag trends in the plane-averaged velocity field of the fluid frame back to a hypothetical value of 0, as done by Keiller and Sleath (1975), who observed effective bed locations of approximately 0.3δ below the particle crests [30]. They also noted a significant departure from the flat-wall behavior in the form of consistent secondary peaks in velocity (compared with those resulting from the plate oscillation) occurring above the sediment bed in the fluid frame. Based on recent simulations in this parameter range, this departure is seen to be the result of vortex structures which form behind sediment elements and subsequently separate from the bed at every cycle [22] [16]. The ejection of vortex structures is consistent with the jet-regime

behavior described by Giménez-Curto et al. (1996) in which oscillatory flow over sediment separates periodically, causing fluid exchange across the effective bed location and inducing dominance of the form stress for flows $\frac{a}{D} < 0.14 \ Re_a^{\frac{3}{4}}$ and $\frac{a}{D} < 500$, which easily applies to the sediment cases discussed here [24].

A minimum energy level is required for particle entrainment to have an observable impact on erosion. Flows within this range of interest are prohibitively expensive to resolve accurately with direct numerical simulations. At commonly found wave periods of 5 to 10 seconds, sand particle sizes of 0.1 to 1.0 mm, and peak fluid velocities of 0.1 to 1.0 meters per second, the computational expense of simulating such a flow can be estimated to be approximately 10^4 to 10^5 times larger than typical small-scale CFD-simulations [20]. Coastal sediment transport being the primary motivation for these simulations, extrapolating results from this study to realistic parameters will be of high importance. The crux of the difficulty of simulating these parameter ranges lies primarily in resolving the disparate scales of wave oscillation amplitude, particle diameter, and the Kolmogorov scales. The difficulty of modeling large-scale oscillations comes with the potential advantage that turbulent time scales may be small enough that the flow can benefit from instantaneous parameterizations of turbulence or open-channel flow models. In light of this, one of the strategies of the early stages of this ongoing investigation will be to compare turbulence and entrainment models of steady, open-channel flows to the simulated oscillatory flow with the hope that similarities found at the low energies of the present simulations will remain valid through extrapolation to relevant parameter regimes.

2.3   Investigation Plan

While the aforementioned work relating statistical assumptions about flow parameters and their relation to particle entrainment in section 2.1 has primarily been applied to open-channel flows, a strong case was made by Mouri et al. (2009) [39] that the probability distribution functions of turbulent properties are consistent between flows with similar relative length scales of consequential fluctuations in relation to the two-point correlation lengths of the velocities, L_u. This will require a novel approach of basing the type of probability distribution function on the scale of the particles relative to the larger scales of turbulence, $\frac{D}{L_u}$. Hofland et al. (2006) [26] and Cheng (2006) [10] also suggest that the relative turbulence intensity of the turbulent properties being used to support the model, $r_\Phi = \frac{\sigma_\Phi}{\bar{\Phi}}$, where Φ is a general flow property, σ_Φ is its standard deviation, and $\bar{\Phi}$ is its mean, should be considered; however, it is possible that these parameters represent the same degree of freedom in determining probability distribution functions of the flow turbulence and this will have similar capabilities. It should be the long-term aim of this overall project to develop analogous

stochastic models for sediment transport in oscillatory flows.

In addition to these purely statistical treatments of the problem, the coherent structures of turbulence will need to be understood with respect to the general flow parameters as they may play a critical role in particle dislodgment; this has already been suggested in research at low and moderate Reynolds numbers [30] [22], and it has yet to be seen how consistently particle motion at higher Reynolds numbers is affected by regular flow events. Furthermore, the action of regularly occurring coherent structures on moving sediment has yet to be observed due to the lack of simulations allowing particle motion in oscillatory flows. Eventually, a simulation along the lines of [8] could be used to observe the effects of such regular structures as well as the specific suspended and bed loads supported by oscillatory flows.

These are far-reaching goals, many of which will not be directly addressed in the present study. Rather, smaller, preliminary goals are addressed which contribute to the ultimate plans of the project.

The objectives of this paper will be to develop an incompressible-flow solver suitable for simulating oscillatory flows and, eventually, many freely moving, fully resolved particles in suspension. Using this solver, the stochastic properties and vortex structures of oscillatory flow over a fixed hexagonal sediment bed at $\frac{D}{\delta} = 6.95$ and $Re_\delta = 95$, 150, and 200 will be studied. It is hypothesized that non-Gaussian bed-velocity distributions will be observed during periods of increasing turbulent kinetic energy and that changes in the probability distribution functions of the bed velocity intensity will be correlated to those of the lift on the particles as a function of phase.

Chapter 3   Development of Numerical Tools

Two major decisions in the development of the solver for this problem were whether it should be structured or unstructured and how rigid sediment particles should be treated. This chapter covers both of these topics in turn, addressing the motivation of the selected method followed by details of its implementation and validation.

3.1   Structured Solver Development

3.1.1   Advantages of a Structured Solver

Unstructured solvers are comprised of polyhedral cells which can be packed arbitrarily closely at regions of interest in the fluid domain. They also easily conform to curved and irregular domain boundaries. This stands in contrast to structured solvers, which feature a Cartesian mesh and therefore have limitations on the variation of cell-packing density. While the advantages of unstructured solvers are substantial, the disadvantages are numerous and turn out to be particularly detrimental in simulating the proposed flows.

Unstructured solvers cannot be simply stored on a Cartesian mesh. The structures of the mesh (comprised of various types of cells, nodes, faces, and boundaries) are typically 1-dimensional and completely independent of location in the fluid domain, so every cell needs to store the indices of connected cells, faces, and nodes separately. Because of this, unstructured solvers require much more memory than structured ones. It has been estimated that 10^8 to 10^9 cells will be needed to generate accurate statistics of particle properties as a function of phase in particle-laden oscillatory flows at the parameter ranges of the present study. Because this cannot be easily achieved on a modest number of processors, the memory requirements and resulting size limitations of unstructured solvers pose a significant disadvantage for this investigation.

The 1-dimensional data structures of an unstructured solver are difficult to learn and generally require more time to develop new numerical tools with. This is particularly burdensome for research projects which involve many individuals working with the solver for short periods of time (as in an academic lab).

Data processing may also prove challenging with unstructured solvers, especially in the case of large-scale, parallelized applications. Because the fluid properties are not spatially ordered, spatially dependent numerical operations cannot be performed without first reordering the data. For instance, a spatial wavenumber decomposition by means of a Fast Fourier Transform (FFT) cannot be accomplished unless data is loaded into arrays with its indices corresponding to its position on an orthogonal set of axes. If an unstructured mesh is comprised of irregular polyhedrons, the fluid properties must first be interpolated to regular positions and then sorted before the FFT can be performed, a task that is memory and time intensive and, therefore, difficult to accomplish at runtime. It is expected that complex data processing will be very important for the proposed project. As an example, spatial correlation functions will be needed to characterize the turbulence properties in the vicinity of the sediment bed to determine if a log-normal probability distribution function is appropriate for a given sediment diameter. For these reasons, a structured solver was implemented.

3.1.2 Cartesian Flow Solver Design

Despite being fundamentally unchanged from its earliest versions in the 1970's, Fortran distinguishes itself as being both efficient with computation of large arrays of data and easy to work with, and remains a natural choice of language for the new solver. It will be outfitted to run with Message Passing Interface protocol so as to scale to tasks of arbitrary size. Being given the opportunity to design a flow-solver from scratch affords the possibility of tailoring different versions of the code for different purposes. Parallel, serial, and long-hand versions of the solver were developed. The long-hand version features momentum and pressure equations which are written out directly in terms of the flow and grid parameters. The serial and long-hand versions are intended to be utilized by new researchers as a learning tool until comfort with the basic elements of the scheme and language are achieved. The serial version will also be useful as a first step in implementing new tools.

A spatially and temporally second-order finite-volume solver was developed for this project, though the spatial accuracy may be improved in the future due to the new solver's spatially consistent storage of flow properties in memory. Flow properties are stored at cell-centers, although face-normal velocities are also stored.

The Navier Stokes and continuity equations describe incompressible flows:

$$\frac{\partial \mathbf{u}}{\partial t} + (\mathbf{u} \cdot \nabla)\,\mathbf{u} = -\frac{1}{\rho}\nabla p + \nu\nabla \cdot (\nabla\mathbf{u}) \tag{3.1}$$

$$\nabla \cdot \mathbf{u} = 0 \tag{3.2}$$

The Navier-Stokes equations are discretized using Adams-Bashforth for the convective terms and Crank-Nicholson for the viscous and pressure terms. The pressure is stored halfway between the timesteps, making this a fractional-timestep method. To simplify the indices, $\mathbf{u} = \{u_x, u_y, u_z\} = \{u, v, w\}$ is used. Equation (3.3) is gives the u-component of the momentum balance, (3.1), written in 2-dimensions on a uniform mesh for clarity:

$$
\frac{u_i^{n+1} - u_i^n}{\Delta t} + \frac{\left(u_{i+\frac{1}{2}}^{n+1} + u_{i+\frac{1}{2}}^n\right)}{4} \frac{\left(u_{i+1}^{n+1} + u_{i+1}^n - u_i^{n+1} - u_i^n\right)}{\Delta x} - \frac{\left(u_{i-\frac{1}{2}}^{n+1} + u_{i-\frac{1}{2}}^n\right)}{4} \frac{\left(u_i^{n+1} + u_i^n - u_{i-1}^{n+1} - u_{i-1}^n\right)}{\Delta x} \quad \cdots
$$

$$
+ \frac{\left(v_{j+\frac{1}{2}}^{n+1} + v_{j+\frac{1}{2}}^n\right)}{4} \frac{\left(u_{j+1}^{n+1} + u_{j+1}^n - u_j^{n+1} - u_j^n\right)}{\Delta y} - \frac{\left(v_{j-\frac{1}{2}}^{n+1} + v_{j-\frac{1}{2}}^n\right)}{4} \frac{\left(u_j^{n+1} + u_j^n - u_{j-1}^{n+1} - u_{j-1}^n\right)}{\Delta y} = \quad \cdots
$$

$$
-\frac{1}{\rho(x_{i+1} - x_{i-1})} \left(p_{i+1}^{n+\frac{1}{2}} - p_{i-1}^{n+\frac{1}{2}}\right) + \frac{\nu}{2(\Delta x)^2} \left(\left(u_{i+1}^n - 2u_i^n + u_{i-1}^n\right) + \left(u_{i+1}^{n+1} - 2u_i^{n+1} + u_{i-1}^{n+1}\right)\right) \cdots
$$

$$
+ \frac{\nu}{2(\Delta y)^2} \left(\left(u_{j+1}^n - 2u_j^n + u_{j-1}^n\right) + \left(u_{j+1}^{n+1} - 2u_j^{n+1} + u_{j-1}^{n+1}\right)\right)
$$

$$(3.3)$$

For reference, the integrated 3-dimensional finite-volume discretization is written out in terms of sums over faces. Using the notation of f_{cc1} for the inside cell-center index with respect to its control volume and f_{cc2} for the outside cell-center index, moving around ρ and introducing $\mu = \nu\rho$, this looks like:

$$
\rho\Delta V \frac{u^{n+1} - u^n}{\Delta t} + \sum_f^{N_{faces}} (\mathbf{A_f} \cdot \hat{\mathbf{n}}) \frac{\rho}{8} \left(u_f^n + u_f^{n+1}\right) * \left(\left(u_{f_{cc1}}^n + u_{f_{cc1}}^{n+1}\right) + \left(u_{f_{cc2}}^n + u_{f_{cc2}}^{n+1}\right)\right) = \dots
$$

$$
- \frac{\Delta V}{x_{i+1} - x_{i-1}} \left(p_{i+1}^{n+\frac{1}{2}} - p_{i-1}^{n+\frac{1}{2}}\right) + \sum_f^{N_{faces}} \frac{1}{2}\mu A_f \left(\left(u_{f_{cc2}}^n - u_{f_{cc1}}^n\right) + \left(u_{f_{cc2}}^{n+1} - u_{f_{cc1}}^{n+1}\right)\right) \qquad (3.4)
$$

This is then solved implicitly for u^{n+1} using a red-black Gauss Seidel method. The pressure contribution is removed (3.5), which gives rise to the Poisson equation under the imposition of continuity (3.7). This is then solved for the correct pressure field using a pressure solver specified by the user at runtime. The pressure field is then used to correct for both the face-based and cell-centered velocities (3.8)(3.9). Because the two velocity fields (face and cell-centered) are updated directly from the pressure field as opposed to each other, the effects of odd-even decoupling observed in some cell-centered solvers are avoided.

$$u^* = u^{n+1} + \frac{\Delta t \quad p_{i+1}^{n+\frac{1}{2}} - p_{i-1}^{n+\frac{1}{2}}}{\rho\left(x_{i+1} - x_{i-1}\right)} \tag{3.5}$$

$$u_{f,i}^* = \frac{u_{i+\frac{1}{2}}^* + u_{i-\frac{1}{2}}^*}{2} \tag{3.6}$$

$$\nabla^2 p = \frac{\rho}{\Delta t}\left(\nabla \cdot \mathbf{u}^*\right) \tag{3.7}$$

$$u_{f,i}^{n+1} = u_{f,i}^* - \frac{\Delta t \quad p_{i+\frac{1}{2}}^{n+\frac{1}{2}} - p_{i-\frac{1}{2}}^{n+\frac{1}{2}}}{\rho \quad x_{i+\frac{1}{2}} - x_{i-\frac{1}{2}}} \tag{3.8}$$

$$u_i^{n+1} = u_i^* - \frac{\Delta t \quad p_{i+1}^{n+\frac{1}{2}} - p_{i-1}^{n+\frac{1}{2}}}{\rho\left(x_{i+1} - x_{i-1}\right)} \tag{3.9}$$

The momentum solver and pressure solver may require multiple successive iterations per timestep; this, however, is not necessary for the simulations discussed here. All simulations are found in practice to have a sufficiently accurate flowfield after a single iteration to proceed to the next timestep.

A caveat to the merits of the structured flow parameters in this solver is that boundary conditions are less efficiently imposed and modified in Cartesian coordinates than generalized 1-dimensional coordinates. It also turns out that the implicit coefficients of the momentum solver are identical for all three momentum equations except at boundaries cells. These points constitute sufficient incentive to develop generalized 1-dimensional data structures for boundary cells and faces. These are used simply as pointers to the underlying structured array and so do not inhibit the advantageous use of spatial ordering. Boundary conditions are enforced more easily by means of this surface structure.

3.1.3   Cartesian Flow Solver Validation

3.1.3.1   Taylor-Green Vortex

The Taylor-Green vortex is a common first trial of a new solver due to its 2-dimensionality, symmetry, existence of a simple analytical solution, and periodic boundary conditions which, because they not have flow across them, can be substituted with slip wall conditions as a test. The flow is described by the following equations:

$$\vec{\mathbf{u}} = U_0 e^{-2\left(\frac{2\pi}{L}\right)^2 \nu t} Sin\left(\frac{2\pi x}{L}\right) Cos\left(\frac{2\pi y}{L}\right) \hat{\mathbf{i}} - e^{-2\left(\frac{2\pi}{L}\right)^2 \nu t} Cos\left(\frac{2\pi x}{L}\right) Sin\left(\frac{2\pi y}{L}\right) \hat{\mathbf{j}} \tag{3.10}$$

$$p = \frac{U_0^2 \rho}{4} e^{-4\left(\frac{2\pi}{L}\right)^2 \nu t} \left[Cos\left(\frac{4\pi x}{L}\right) + Cos\left(\frac{4\pi y}{L}\right)\right], \tag{3.11}$$

where U_0 is the maximum velocity, and L is the length of an edge of the domain, which must be consistent between dimensions, The flowfield is a lattice of vortices with staggered directions of rotation. The solution is separable in time and space, which is another advantage of this case as many implementation errors will cause changes in the direction of flow field in time which are easily observed. The exponential decay of the velocity field can be easily observed on a log-linear plot. This case was run at $Re = 100$ on a 128×128 uniform grid with slip boundaries and $\nu = 0.01$, $L = 2.0$, and $\Delta t = 5 \times 10^{-3}$. Table 3.1 lists the point-by-point error of the x component of velocity on the horizontal line $y = 0.75$. The error is in the range of 10^{-4} to 10^{-5} when normalized by the largest value found in the correct solution on the line. The Taylor-Green vortex was also run on this solver for a grid refinement study, see section 3.1.3.4.
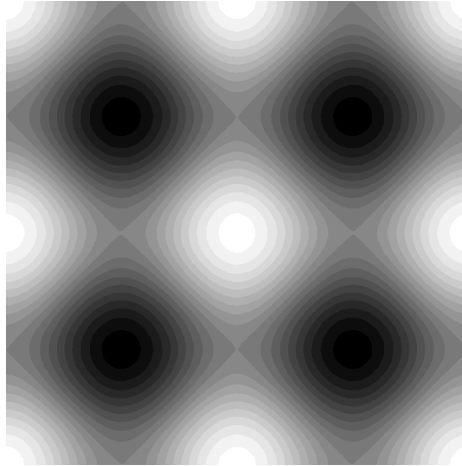
(a) The pressure field of the Taylor-Green vortex solution.
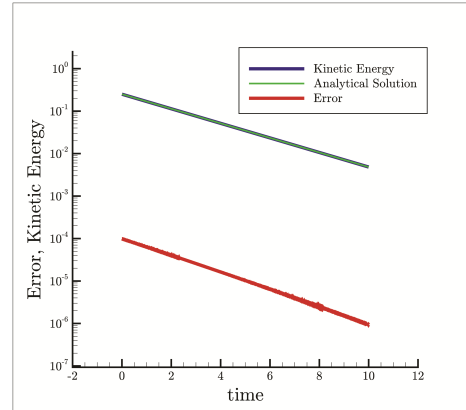
(b) A log-linear plot of exponential kinetic energy decay of the Taylor-Green vortex.

Figure 3.1: A validation study of the new solver running a Taylor-Green vortex of $Re = 100$.

x	correct u_x	present u_x	Δu_x
0.0	0.0000000	-0.0000002	0.0000002
0.1	-0.0042164	-0.0042170	0.0000010
0.2	-0.0080201	-0.0080206	0.0000004
0.3	-0.0110387	-0.0110402	0.0000015
0.4	-0.0129767	-0.0129774	0.0000007
0.5	-0.0136445	-0.0136466	0.0000021
0.6	-0.0129767	-0.0129773	0.0000006
0.7	-0.0110387	-0.0110405	0.0000018
0.8	-0.0080201	-0.0080203	0.0000003
0.9	-0.0042164	-0.0042172	0.0000008
1.0	0.0000000	0.0000001	0.0000001

Table 3.1: Comparison of u_x along the horizontal line defined by $y = 0.75$ on a 2D Taylor-Green vortex with $\nu = 0.1$, $t = 20.0$, $L_x = L_y = 2.0$, $N_x = N_y = 250$ and $\Delta t = 0.001$.

3.1.3.2   Lid-Driven Cavity

A 2-dimensional lid-driven cavity provided a first test of stationary and moving wall conditions as well as a non-uniform mesh treatment. The $Re = 1000$ case of Botella and Peyret (1998) was chosen as a benchmark for the problem. The geometry of this was a 1×1 square with four wall boundaries. The fluid is initially at rest, and the top wall is kept moving at a constant speed of 1. The solver was run at a constant timestep of $\Delta t = 5 \times 10^{-3}$; a plot of kinetic energy indicated the solution was sufficiently converged after 10000 timesteps. Initially, a uniform 128×128 mesh was used for this case but converged on a slightly different flow compared with the published solution. Botella and Peyret used a spectral solver, which may have an inherent advantage in resolving the difficult gradients at the corners of the moving wall. A non-uniform 128×128 mesh was required in the new solver to produce a flow-field nearly identical to that of the benchmark case (see figure 3.2b) compared with figure 2 in [4]. A slight error still exists, and judging by the trends seen between the uniform and non-uniform meshes, the sharp gradients at the $z = 1.0$ corners are still not being resolved quite as well as in the benchmark. Table 3.2 lists values of the vertical velocity component along the horizontal centerline of the flow. They prove to be in good agreement with the published solution; the peak error among these points does not exceed 0.6% of the benchmark value.

3.1.3.3   Turbulent Channel

The turbulent-channel case used by Kim et al. (1987) [31] was run to validate the accuracy of turbulent flows on the new solver. The Reynolds number of this case, defined as $Re_\tau = \frac{u_\tau \delta}{\nu}$,
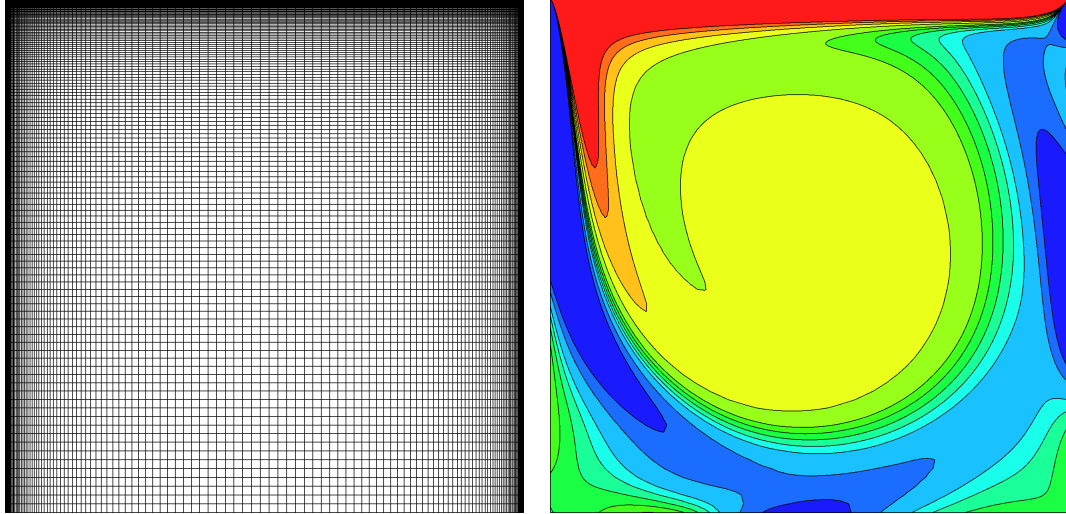
(a) A non-uniform mesh was required to achieve vorticity contours comparable to the 128×128 benchmark [4].

(b) Vorticity contour lines at 5, 4, 3, 2, 1, 0.5, 0.0, -0.5, -1, -2, -3 for comparison with [4].

Figure 3.2: A lid-driven cavity validation case at $Re = 1000$ for comparison with Botella and Peyret (1998) [4].
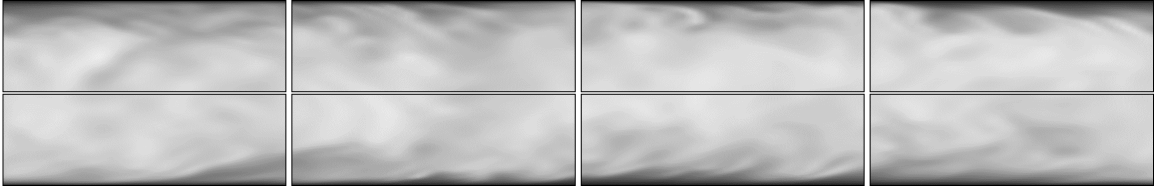
Figure 3.3: Instantaneous u_x velocity field of the turbulent channel case, $Re_{u_\tau} = 180$

was 180. The flow was initialized to uniform flow of $\frac{u}{u_m} = 20$ across the channel with substantial perturbations imposed. The timestep was run at constant values with the CFL below 1.0. The flow was maintained by means of volumetric forcing; spanwise and streamwise boundary conditions are therefore periodic. All fluid properties are normalized by the mean wall shear stress, τ_w, and wall velocity, $u_\tau = \sqrt{\frac{\tau_w}{\rho}}$, and as a result, the volumetric forcing only depends on the flow geometry and $\nu = Re_\tau^{-1}$. The original study used a grid spacing with a sinusoidal dependence: $y = \text{Cos}\,[2\pi\eta]$ where $\eta = \frac{y}{L_y}$. The present study utilizes hyperbolic functions to define the mesh spacing in order to lessen the extremity of the aspect ratio near the walls: $y = (L_y \text{Coth}\,[2]\,\text{Tanh}\,[4\eta - 2] + 1)\,/2$. An instantaneous plane of the streamwise-velocity field is depicted in figure 3.3.

x	u_z [4]	u_z	Δu_z
1.0000	0.00000	-0.00000	0.00000
0.9688	-0.22792	-0.22752	0.00040
0.9609	-0.29368	-0.29326	0.00043
0.9531	-0.35532	-0.35500	0.00032
0.9453	-0.41038	-0.41007	0.00031
0.9063	-0.52644	-0.52518	0.00126
0.8594	-0.42645	-0.42505	0.00140
0.8047	-0.32021	-0.31885	0.00186
0.5000	0.02579	0.02583	0.00004
0.2344	0.32536	0.32457	-0.00082
0.2266	0.33399	0.33313	-0.00089
0.1563	0.37692	0.37493	-0.00199
0.0938	0.33304	0.33125	-0.00179
0.0781	0.30991	0.30831	-0.00160
0.0703	0.29012	0.29481	0.00146
0.0625	0.27485	0.27930	0.00141
0.0000	0.00000	0.00000	0.00000

Table 3.2: Comparison of u_z along the horizontal centerline of the lid-driven cavity at $Re = 1000$ compared with values from Botella and Peyret (1998) [4].

	present study	Kim et al. (1987) [31]
$\frac{U_m}{u_\tau}$	15.89	15.63
$\frac{U_c}{u_\tau}$	18.62	18.20
$\frac{U_c}{u_m}$	1.17	1.16
C_f	7.92×10^{-3}	8.18×10^{-3}
C_{f_0}	5.77×10^{-3}	6.04×10^{-3}

Table 3.3: Comparison of mean flow properties of a turbulent channel of at $Re_\tau = \frac{u_\tau \delta}{\nu} = 180$ with simulation parameters chosen to replicate Kim et al (1987) [31] with the exception of the mesh stretching, which is defined by hyperbolic functions as opposed to sinusoidal functions. C_f is the friction factor defined with respect to the mean velocity, while C_{f_0} is defined with respect to the centerline velocity.

The mean flow properties, shown in table 3.3, deviate slightly from the benchmark case of [31]. The non-dimensional mean velocity, for instance, is 15.89 as opposed to 15.63 in Kim et al., 1.7% larger. Profiles of plane-averaged values of u_{rms}, v_{rms}, and w_{rms} are shown in figure 3.4 which can be compared with figure 6a in [31]. While the profiles of the u and v components appear to be in agreement with the benchmark up to a small correction factor, the present-case w component approaches zero less rapidly near the wall. Possible explanations of this are the use of a different mesh as well as the use of a finite-volume method in the present case as opposed to a spectral method of
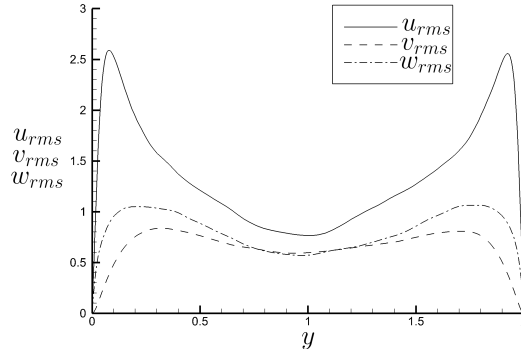
Figure 3.4: Profiles of plane-averaged values of u_{rms}, v_{rms}, and w_{rms} versus the y coordinate (between the walls) of the turbulent channel case, $Re_{u_\tau} = 180$

Kim et al. (1987), which would be better suited to handle the grid stretching near the wall. Aspect ratios of approximately 50 to 1 are found in the present case at the cells bordering the walls. This difference may be responsible for the observed disparities in mean velocities between the present case and the benchmark.

Outside of the error in the solution, trends of the flow properties and turbulent fluctuation profiles are in general agreement with Kim et al. 1987 [31]. While more testing is needed on turbulent cases, this simulation suggests turbulence is accurately simulated in the present solver.

3.1.3.4   Grid-Refinement Study with a Taylor-Green Vortex

The Taylor-Green vortex was revisited to perform a grid-refinement study due to its ease of execution. Uniform meshes of 50×50, 100×100, 250×250, and 500×500 cells were compared against a validation case of 1000×1000 cells. All simulations used the same timestep of 10^{-3} and were run for 2000 iterations. Other parameters were $\nu = 0.001$, $L_x = L_y = 2.0$, and $U_0 = 0$. Care was taken to select a timestep which would keep the CFL parameter of the validation case below 1. The pressure of the validation case was interpolated to the meshes of the smaller cases where the absolute value of error was computed. The integrated percent error is plotted in figures 3.5a and 3.5b. This is equivalent to the first norm of the normalized pressure field, making the solution independent of the scale of the pressure. The solutions can be seen to be at least second-order.
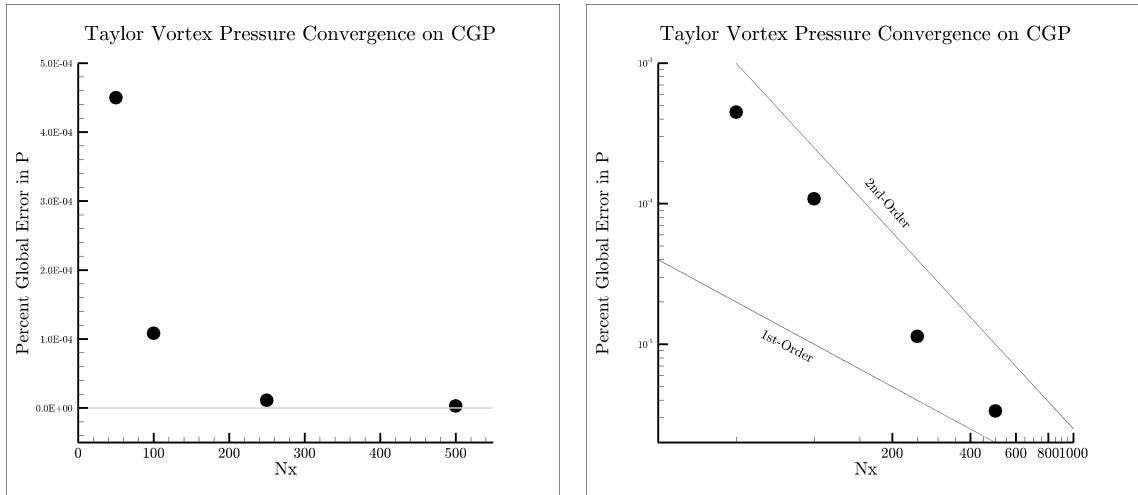
(a) The absolute normalized error in pressure.   (b) Spacial accuracy on a log-log plot of error.

Figure 3.5: A refinement study of the new structured solver conducted on a Taylor-Green vortex at $Re = 100$.

3.2 The Immersed-Boundary Solver

3.2.1 Body-Fitted and Immersed-Boundary Methods

Two common methods of simulating flow around rigid bodies exist, both are arguably straightforward. One is to define a mesh which conforms to the body in question and impose wall conditions on the boundary. This then requires that the cell pattern be changed to accommodating moving bodies. The alternative is much more conducive to moving bodies: that rigidity be imposed upon the fluid domain by requiring the fluid velocity to go to zero within the body. Such techniques are known as immersed-boundary methods, or IBMs, and utilize a variety of different approaches to accomplishing rigidity [47] [56] [37]. In these methods, rigid-body translation and rotation are determined by applying basic Newtonian mechanics.

3.2.2 The Fictitious Domain Method

The fictitious-domain method (FDM) was chosen as a first immersed-boundary implementation for the new solver. FDM features a superlattice of Lagrangian material points subdividing each cell volume. To impose rigidity, fluid properties are first interpolated to the material points, where the force necessary to cancel the local velocity over that timestep is computed. For interpolation, the three-point delta function proposed by Roma et al. (1999) is used [43]:

$$
\begin{aligned}
&= \frac{1}{3} \ \left[1 + \sqrt{-3r^2 + 1} \right] && |r| < 0.5 && (3.12) \\
\phi(r) \quad &= \frac{1}{6} \ \left[5 - 3\,|r| - \sqrt{-3\left(1 - |r|\right)^2 + 1} \right] && 0.5 \leq |r| \leq 1.5 \\
&= 0 && 1.5 < |r| \ ,
\end{aligned}
$$

which conserves the magnitude and location of the interpolated property, attempts to minimize the relative location of the grid's impact on the flow, and has continuous first derivatives. This force is then interpolated back to the fluid domain, where it is added as a source term in the momentum equations. As with the momentum-pressure solver combination, this can be iterated within each timestep for maximal convergence, but in practice, a single iteration produces accurate convergent properties. While the rigid body is represented with a sharp stair-step pattern on the Lagrangian superlattice, it becomes diffuse when interpolated onto the fluid domain (see figure 3.6). The blurriness is diffused over three fluid-cell discretizations as a result of the delta-function interpolation. Apte and Finn (2012) make a detailed comparison between FDM and grid-fitted techniques and find that FDM requires fewer cells to attain a fixed level of error in the flow field [1].

3.2.3 Immersed-Boundary Solver Validation

Like the general fluid solver, the interpolation function of the immersed-boundary solver is second-order accurate in space. The treatment of the fluid interface is less clear, specifically whether or not the discrete material-point assignment is a second-order approximation of the analytical definition of the cylinder. Significant local error may exist depending on the relative position of the surface definition and the superlattice; however, convergence is still expected to be second-order.

3.2.3.1 Grid-Refinement with a Confined-Cylinder Case

The local spatial accuracy of this implementation of FDM was tested by means of a grid refinement study on a confined flow over a cylinder, the same technique used by Mittal et al (2008) [38]. The domain for this simulation is 2 by 2 units in two dimenstions with a centered cylinder of unit diameter subjected to a uniform channel-flow at the inlet on one of its sides, and an outlet on the opposite side. It is unclear what the other two boundaries are intended to be in [38]; the streamwise velocity contours in their figure 8a suggest a wall moving at the velocity of the inlet fluid; however, it is unlikely they would have selected these conditions without explaining them, so it may

(a) The material point superlattice is defined for a rigid body based on an analytical definition of the surface. The object is represented as a clearly defined stair-step pattern on the superlattice.

(b) Once interpolated to the fluid domain via a forcing function, the rigid-body interface becomes wavy and diffuse. The use of a finer discretization of the superlattice than the fluid mesh can eliminate much of the waviness, but the blurred boundary is tied to the 3-point interpolation function.

Figure 3.6: The use of material points in the Fictitious-Domain Method.

be a mistake. Periodic conditions were used for this study. Resolutions of 400×400, 200×200, 100×100, and 50×50 were compared with a master case of 800×800. Error in the domain should be dominated by the local variations in the flow field around the surface (see figure 3.7b, analogous to figure 8 in [38]). The L_1, L_2, and L_∞ norms of the error in u_x are plotted against the grid resolution on a log-log plot, shown in figure 3.7a (analogous to figure 9 in [38]).

The error in u_x depicted in 3.7b is consistent with that depicted in figure 4c of Apte and Finn (2012) [1] and has similar qualities near the object surface, particularly around peak error, to figure 8b of Mittal et al. (2008) [38]. The overall magnitude of error is greater in our case, which may be due to the blurred representation of the interface created by the fictitious domain method; however, this distinction is obscured by the apparent use of a different boundary condition in Mittal et al. This plot verifies that the global error is dominated by local error near the particle interface, which supports the assertion that these simulations indicate the spatial accuracy of the fictitious-domain implementation of the present solver. The convergence of the norms of the error are shown in figure

(a) The norms of error of the streamwise velocity around a confined cylinder as a function of grid resolution. The spatial accuracy of the solver can be seen to converge to second-order.

(b) The error in the streamwise velocity around the cylinder interface on a 200×200 grid computed with an 800×800 grid solution.
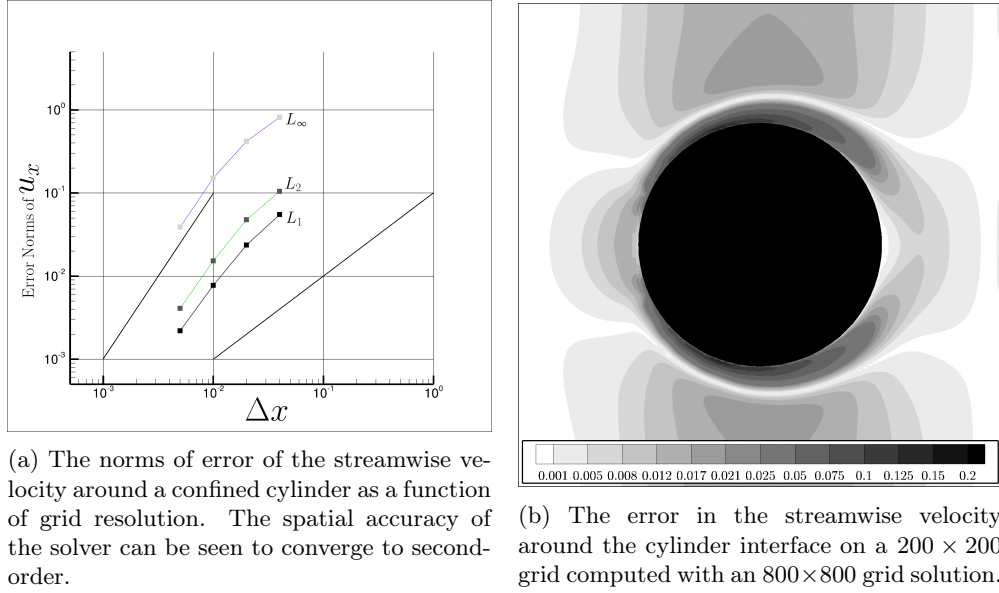
Figure 3.7: A grid refinement study of the spatial accuracy of the new rigid-body solver conducted on the confined flow over a sphere. The local error at the rigid-body interface can be seen to be dominant which indicates the second-order trend is a reflection of the fictitious-domain implementation.

3.7a which confirm the immersed-boundary treatment is spatially second-order accurate.

3.2.3.2 Unconfined Flow over a Cylinder

In addition to a convergence study, flow over a unit cylinder in an open flow of relative size 40×40 at $Re = \frac{U_{in} D_{cyl}}{\nu} = 40$, 100, 300, and 1000 were run with $\Delta t = 0.005$, and $\frac{D}{\Delta x} = 60$ on a 500×500 mesh. At the highest three Reynolds numbers, a Kármán vortex street forms in the wake of the sphere.

	100	300	1000
present study	0.167	0.212	0.239
Apte et al. (2009) [2]	0.165	0.212	0.238
Mittal et al. (2008) [38]	0.165	0.21	0.231

Table 3.4: Strouhal numbers for flow over an unconfined cylinder at $Re = 100$, 300, and 1000 measured by oscillations in the lift coefficient.

The fully developed unsteady drag coefficient is compared against values in literature in table

	40	100	300	1000
present study	1.55	1.36	1.41	1.55
Apte et al. (2009) [2]	1.54	1.36	1.41	1.50
Mittal et al. (2008) [38]	1.53	1.35	1.36	1.45

Table 3.5: Drag coefficients for flow over an unconfined cylinder at $Re = 100$, 300, and 1000.

3.5. Strouhol numbers are also compared in table 3.4. The drag on the cylinder at $Re = 1000$ and the Strouhal number at $Re = 100$ considerably deviate from both of the other values shown. One possible explanation of this is that the flow was not fully developed and needed to run longer for accurate comparison. The small disparity between the present drag coefficent at $Re = 40$ and that of Apte et al. (2009) [2] is of interest because the flow was clearly fully developed in the present study and the solver used by [2] is almost identical to the present one. The difference may be ascribed to different resolutions of material point density, which in one-dimension are 3 to 1 in the present case as opposed to 4 to 1 in [2]. Outside of these differences, the values of the present solver are in acceptable agreement with the published values.

The drag evolution and vorticity contours of the $Re = 1000$ case, shown in figure 3.8 are in general agreement with figures 7c and 8d of Apte et al. (2009) [2].
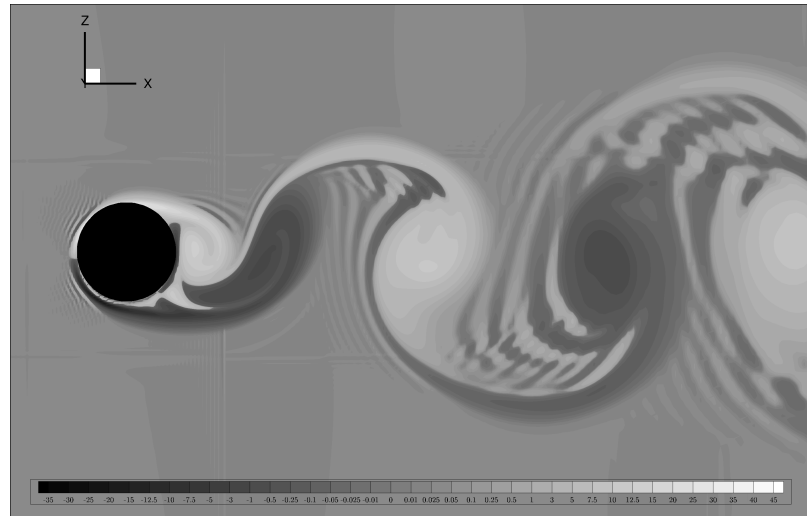
(a) vorticity contours
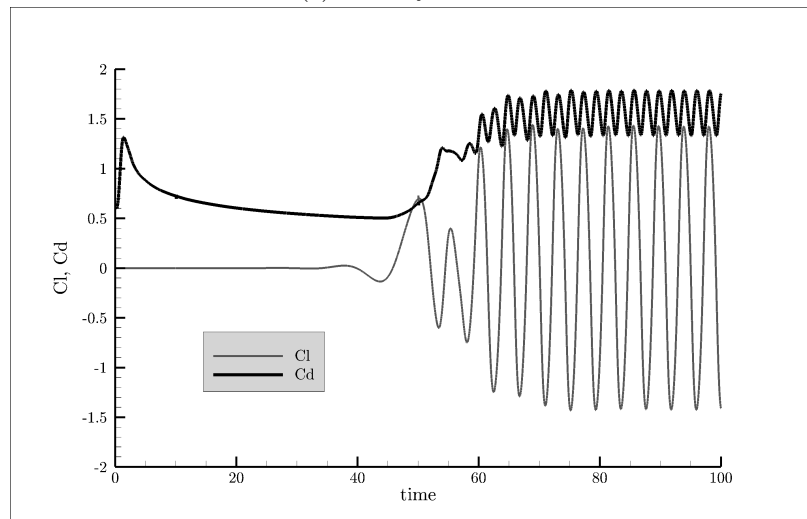
(b) developing drag and lift coefficients

Figure 3.8: An unconfined-cylinder case with $Re_D = 1000$ on a stretched 500×500 mesh run on the new structured rigid-body solver. Here, $D = 1$, $L_x = L_y = 40$, $\frac{D}{\Delta x} = 60$, $\nu = 0.001$, and $\Delta t = 0.005$.

3.3 Future Solver Development and Use

Although the core fluid solver has be shown to run accurately, many tools will need to be implemented for the study of sediment transport in oscillatory flows. First among these is an efficient pressure solver. The fluid solver as a whole may be capable of performing very large simulations in
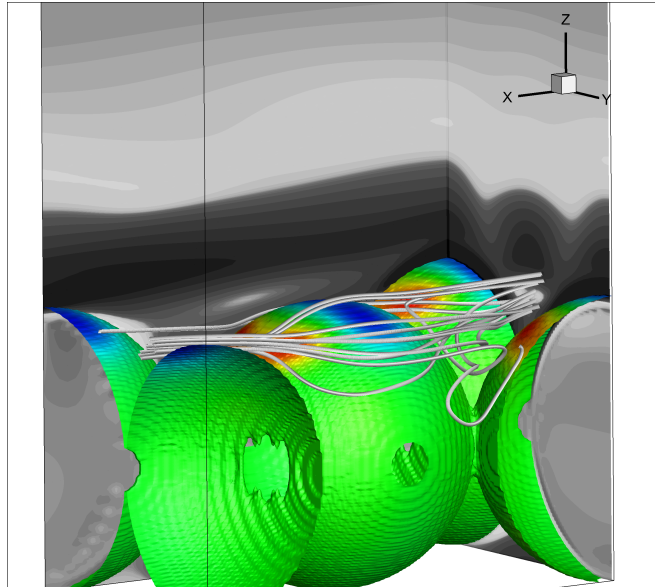
Figure 3.9: A small sediment case run on the new solver at $Re_\delta = 95$. The new solver is expected to be used to execute large simulations of this geometry in the near future.

space and memory, but it currently executes them too slowly to be a desirable choice. Initially, a BCG-STAB pressure solver will be implemented. Eventually the code will be linked to an external, open-source multigrid package. These options will hopefully improve runtimes by a factor of $\mathcal{O}(10^1)$.

A second important implementation will be an improved immersed-boundary treatment of rigid bodies which features more accurate flow reconstruction at the fluid-body interface and unambiguous second-order spatial accuracy. This is likely to be similar to the Sharp Interface Method of Mittal et al. (2008) [38]. This will require some modifications to interprocessor communications as more fluid cells will need to be made available to such an immersed-boundary method. Once this is accomplished, a four-point interpolation stencil will also be introduced for discrete interpolations in an effort to mitigate anticipated unphysical force perturbations resulting from smaller stencils when applied to rigid bodies moving across Cartesian grids.

The future of this project is likely to include simulations of large numbers of suspended interacting sediment particles, so the new rigid-body solver will be implemented to allow for moving bodies. State-of-the-art treatment of particle collisions will need to be used to ensure the accuracy of simulations of particle-laden flow, such as the methods proposed by Simeonov and Calantoni (2012) [48]. Additionally, if particles are expected to be moving and the number of particles per processor is

small (10) then individual processors instantaneously burdened with larger particle numbers will perform rigid-body operations more slowly than others. This effect will be compensated for by incorporating dynamic processor redistribution of the domain such that the particle load is shared evenly.

Although not directly built into the solver, post-processing tools will need to be written to act on binary representations of flow data directly in Fortran. The lack of such tools in the current solver has been in part due to its spatially inconsistent ordering of data in memory and has resulted in limited and less efficient processing options on the data sets involved in this study.

Finally, an assortment of other tools can be implemented either in post processing routines or the main solver when the need arises. These include forward and backward flow mapping [19], which would be paired with the task of extending this technique to periodic boundary conditions, spatial Fast Fourier Transforms (FFTs), correlations functions, vortex detection, and generalized spatial differentiation of flow parameters.

Chapter 4 Computational Setup of Problem

The simulations run for this thesis all feature 8 spherical particles of $\frac{D}{\delta} = 6.95$. The packing configuration is a uniform hexagonal pattern of spheres, which are in contact with one another. Sediment elements have neighbors in the spanwise direction as well as thirty degrees above and below the streamwise direction (see figure 4.1). Simulations were performed for $Re_\delta = 95$, 150, and 200. The motivation for exploring the $Re_\delta = 95$, $\frac{D}{\delta} = 6.95$ flow is for comparison with [16, 22, 30], which also explore this choice of parameters. The higher Reynolds numbers were intended to probe developing and fully turbulent parameter regimes, as predicted by [52] (see figure 5.1). $\frac{D}{\delta}$ was kept constant to isolate the effects of the changing Reynolds number. All units used are non-dimensional unless otherwise specified, being scaled by δ for length and T for time. Table 4.1 provides the domain and mesh sizes for each of these cases. Table 4.2 lists a hypothetical set of parameters in SI units for a realistic period of 5 seconds.

Boundary conditions are periodic in the streamwise and spanwise directions. The sediment elements are resting on a flat wall and a slip condition is imposed at the top of the domain. Wave motion is imposed on the fluid with a pressure gradient of $\rho\omega U_\infty Cos(\omega t)$, which is treated as an explicit forcing term in the momentum balance and does not affect cells located within rigid bodies. Note the choice of imposing oscillatory motion with a cosine function results in $u_\infty(\phi) \propto Sin(\phi)$, while frequently cited papers on this topic typically do the opposite. This choice was made so that the fluid can be initialized as stationary at $t = 0$. As a result of this, the data presented herein will be at a 90° phase lead compared to most of the plots in the related literature [16, 22, 30]. The simulations were run at a constant CFL of .7 to .9 until fully developed, at which point they were run at a constant timestep, with CFL peaking near 1.0 for data collection.

Because the flow is both oscillatory and spatially regular, a system of phase-space averaging is introduced:

$$\bar{\Phi}(\phi, r) = \frac{1}{N_{spheres}} \sum_{\vec{r}}^{N_{spheres}} \left(\frac{1}{N_{cycles}} \sum_{c=0}^{N_{cycles}-1} \left(\Phi(\phi + 2\pi c, r) \right) \right) , \qquad (4.1)$$

where Φ is the flow parameter being phase-space averaged and is associated with the nearest sphere for the spatial summation. Based on this average, instantaneous properties are decomposed into a phase-space-averaged component and an instantaneous fluctuating component: $\Phi(\phi) = \bar{\Phi}(\phi) + \Phi'(\phi)$.

This greatly increases the difficulty of gathering statistically meaningful sample sizes and the complexity of analyzing otherwise simple flow properties. It also requires vast amounts of memory to average the phases in high-resolution at runtime, which was done for these simulations. Phase-space averaging was begun after 5 iterations when the flow was deemed fully developed based on a converged periodic drag and fluid profile. The Shields parameter is not relevant as the sediment bed will be held fixed for this set of simulations. Because particle motion is disabled, the bed-slope is also irrelevant. Only purely oscillatory flow is investigated.

Re_δ	$\frac{D}{\delta}$	N_x	$\frac{\Delta x}{\Delta y}$	N_y	N_z	L_x	L_y	L_z	N_{cells}	$\frac{N_y}{D}$	Turb
95	6.95	208	1	120	172	24.1δ	13.9δ	30δ	4.3×10^6	60	no
150	6.95	172	2	200	288	24.1δ	13.9δ	30δ	10.0×10^6	100	yes
200	6.95	208	2	240	344	24.1δ	13.9δ	30δ	17.2×10^6	120	yes

Table 4.1: Simulation parameters for the 3 cases explored in this study.

Re_δ	U_∞	δ	D
95	7.5 cm/sec	1.26 mm	8.76 mm
150	11.9 cm/sec	1.26 mm	8.76 mm
200	15.8 cm/sec	1.26 mm	8.76 mm

Table 4.2: Hypothetical conditions for a flow in water with $T = 5$ seconds corresponding to the three cases simulated in this study

Convergence studies were tested at $Re_\delta = 95$ on a quarter domain, i.e. 2×1 spheres, with resolutions of $\frac{N_y}{D} = 20, 30, 40, 60,$ and 80 and a $\frac{N_y}{D} = 120$ validation case. This was done for both uniform Cartesian meshes, and meshes stretched to twice as long in the streamwise direction, that is, to half as many points within L_x. In all cases, the spanwise discretization was held constant at the listed values. It was found that the stretched grid gave comparable performance to the uniform grid; the stretched grid was used primarily due to the benefits of having a less restrictive CFL condition (as opposed to the benefit of reducing the cell count by a factor of two). This permitted the simulations to run almost twice as fast as they would on the uniform mesh. Results from the convergence study may be found in figure 4.2a, which verifies the existing solver is second-order accurate in this particular case. In addition to this relative stretched-mesh analysis, the convergence study provided good estimates on the absolute error of different flow parameters (figure 4.2b). Global error in second-order flow parameters was kept below 1%, while global error in the vorticity was kept below 5%. This occurred at $\frac{N_y}{D} = 60$ in the $Re_\delta = 95$ case. It was originally the intention to replicate the turbulence conditions reported in Fornarelli and Vittori (2009) [22] and use the relation $\eta \propto Re_\delta^{-\frac{3}{4}}$ assuming the mixing length is constant; however, the flow ended up being laminar (see discussion

in section 5.1), so a safety margin of 2 was assumed and the turbulent relation was used anyway, perhaps unjustifiably, but still resulting more finely resolved flow at that Reynolds number than in the limited literature on this particular case.
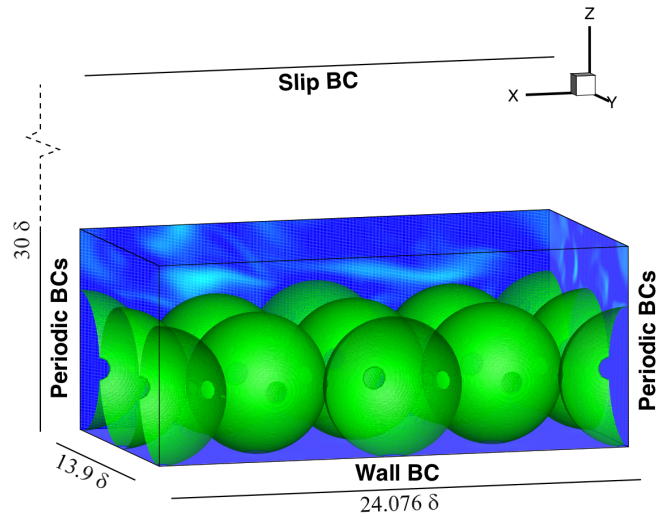
Figure 4.1: An image of the flow geometry from all cases: $Re_\delta = 95$, 150, and 200.

(a) Order of spatial accuracy.

(b) Absolute normalized spatial error.
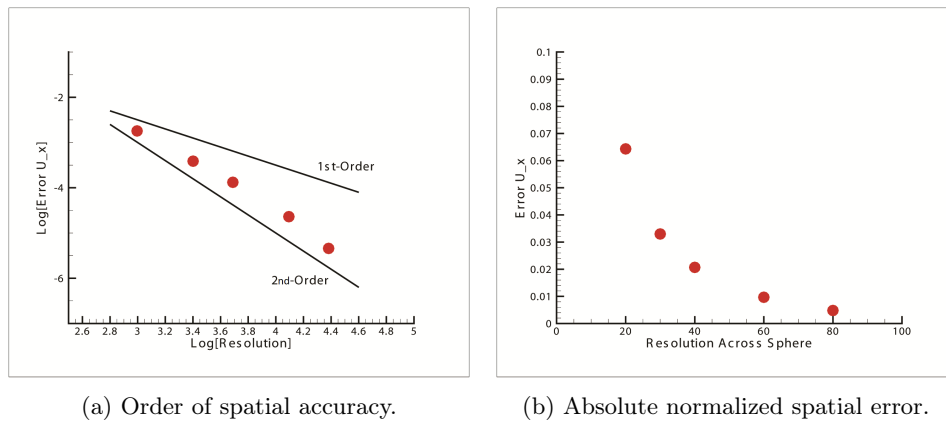
Figure 4.2: A grid refinement study of the old solver performed directly on a small $Re_\delta = 95$ oscillatory-flow case with 2 spheres. The old solver was used to run the simulations presented in this paper.

Chapter 5   Results and Discussion

5.1   Comparison with Existing Published Work

As mentioned in section 4, the $Re_\delta = 95$ case was chosen primarily to allow for comparison with the experimental work of Keiller and Sleath (1975), hereafter K&S [30], as well as the fully resolved simulations of Fornarelli and Vittori (2009), hereafter F&V [22], and Ding and Zhang (2010), hereafter D&Z [16]. This case is modeled specifically after experiment #41 in K&S. It is worth noting that the flow is described as laminar in the original study and that the sediment elements are in contact with one another just as they are in the present work, while F&V and D&Z have small gaps of 1.05δ and 1.135δ respectively between their spheres. The other difference in geometry is that K&S originally used spheres glued on a flat surface to simulate the effects of a sediment bed, while F&V constrained themselves to using semispheres in their simulations. Both D&Z and the present study utilize a single layer of whole spheres. To summarize, the present simulations should actually be better recreations of the original experiment and actual coastal environments than the recent simulations of F&V and D&Z due to the contact between spheres as well as the inclusion of sphere bottoms and the surrounding pore space. The latter advantage is bound to be partially compromised though, as the pore space was fully laminar in all of our simulations due to restrictions of the lower wall. It may be possible to use the instantaneous pore-space Reynolds number to estimate the transition to turbulence in the pore space:

$$Re_p \equiv \frac{u_p d_p}{\nu} \tag{5.1}$$

$$u_p \equiv \frac{1}{A} \int \bar{u}_b dA, \tag{5.2}$$

where A is the cross-sectional area of the pores-pace channel, d_p is the diameter of the channel, and u_p is the pore space velocity. The present $Re_\delta = 200$ case of $50 < Re_p < 100$ may breach the threshold of turbulence near $Re_p = 300$ [27] if another layer of sediment were included the higher Reynolds numbers, depending on the specifics of the vertical packing alignment (see section 5.4).

The transition to turbulence of oscillatory flow over a flat plate is reported by Vittori and Verzicco (1998) to feature intermittent turbulence [60]. Specifically, turbulence occurs at peak velocities which decays to laminar flow as the velocity approaches reversal. For flat beds, K&S suggest that the

transition is gradual, and that the early stages of turbulence have mean-flow properties dominated by "laminar processes such as vortex formation and decay". Here, turbulence is defined with respect to the phase-space-averaged flow properties, that is, a fully laminar flow is identical from cycle to cycle, but not phase to phase. A fully turbulent flow, for the purposes of this study, is one in which variations from the phase-space-averaged flow properties exist at all phases of the cycle, and an intermittent regime, if one exists, would be characterized by variations from the phase-space-averaged properties near the peak velocities of the cycle and a return to average properties near flow reversal.

Like experiment #41 of K&S, the simulation at $Re_\delta = 95$ produced laminar results. This stands in contrast to the turbulence noted by F&V. This disparity suggests that spacing between spheres must be a relevant length scale in characterizing the flow, specifically the transition to turbulence, signaling a possible subject for future study of addressing the flow differences as a function of this spacing. Efforts were made to perturb the flow at this Reynolds number; however, despite relatively strong forcing at a variety of wavenumbers, the solutions decayed back to a laminar state within a period or so. The lack of flow disturbances at $Re_\delta = 95$ in the present study does not conform to the empirical models suggested in equations 5 and 7 of Sleath (1988) [52] (see figure 5.1). This is likely due to the uniformity of the geometry in the present simulations. Particle irregularity should be able to sustain turbulence at lower Re_δ. Regardless, the onset of turbulence in these simulations is more sudden than Sleath's models would suggest; at $\frac{D}{\delta} = 6.95$, the models have a transitional range of approximately 200 Re_δ, which is large when compared with the upper bound of 55 in between the laminar $Re_\delta = 95$ and turbulent $Re_\delta = 150$ cases presented here. This sudden onset of turbulence is consistent with observations that a uniform sediment bed geometry may give rise to small transitional regimes [9, 29].

As mentioned in section 2.2, literature pertaining to this topic frequently uses an alternative frame of reference consistent with the experiments of K&S, in which an oscillating sediment bed is interacting with a stationary body of fluid, termed the fluid-frame here. Figures 5.2a, 5.2b, 5.3a, and 5.3b will be presented in this frame to allow for direct comparison with K&S. The use of u^* denotes the velocity in this frame. The transformation of frames of reference is only correct to an approximation for three-dimensional flows and should not be viewed as validation.

Figure 5.2a, depicts the variation of the peak phase-space-averaged velocity (in the fluid frame) with respect to the height above the sediment crest. Data presented are from F&V, D&Z, K&S, and the present study, where this type of plot was first published. Based on this plot, the present data are a good fit for K&S and generally better than both F&V and D&Z. This is probably due to the use of touching spheres, which F&V and D&Z did not use. Figure 5.2b tracks the phase at which peak velocity is recorded (in the fluid frame) as a function of height above the sphere. An ideal
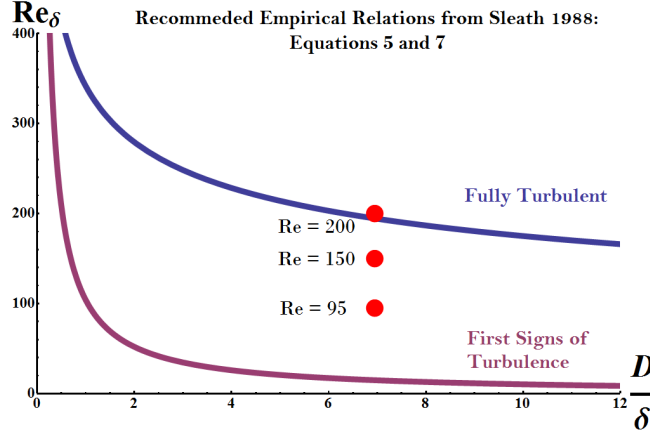
Figure 5.1: Recommended empirical relations of the transition to turbulence of oscillatory flow over sediment from Sleath (1988) [52].

Stokes flow over a flat plate oscillating in its own plane would have a linear dependence between the phase of the peak velocity and the height above the surface, so the vertical trend occurring in the range of $0.1 < \frac{z}{\delta} < 0.3$ is a clear departure from such a dependence and must be a direct result the inclusion of surface roughness of the sediment. The peak velocity of the vertically trending region corresponds to the secondary peak of the fluid-frame velocity being greater than the primary peak. The maximum velocity for which this is the case occurs somewhere in the range $0.25 < \frac{z}{\delta} < 0.28$, which can be compared to the fits of the maximum height in figure 5 of K&S. The present study's value is lower than that of K&S yet conforms to the empirical fit nearly as well. This suggests that the departure from K&S is not in disagreement with their findings as a whole.

Figure 5.3a shows phase-space-averaged velocity in the fluid frame as a function of phase at varying heights directly above the sphere crests. Because this plot is in the oscillating fluid frame, the velocity should approach a sinusoidal temporal profile in the limit of $\beta z \to 0$ (where $\beta = \frac{1}{\delta}$ is adopted for consistency with K&S). In K&S (figure 2), varying degrees of waviness are observed as opposed to the distinct oscillations further from the wall during the decelerating phases in the present study; this discrepancy is most prominent far from the crest where the velocity approaches zero. Oscillations occurring at $\beta z = 0.2$, the closest probe to the wall, are another departure from the present findings in figure 5.3, where the velocity approaches a smooth sinusoidal profile. The oscillations closest to the crest are of approximately the same frequency as those occurring at later phases at all distances from the crests in the present simulation. The lack of this in the present findings may indicate insufficient resolution near the sphere surface; however, it should be noted that, according to K&S, the wall was estimated to have an unphysical impact on the measurements
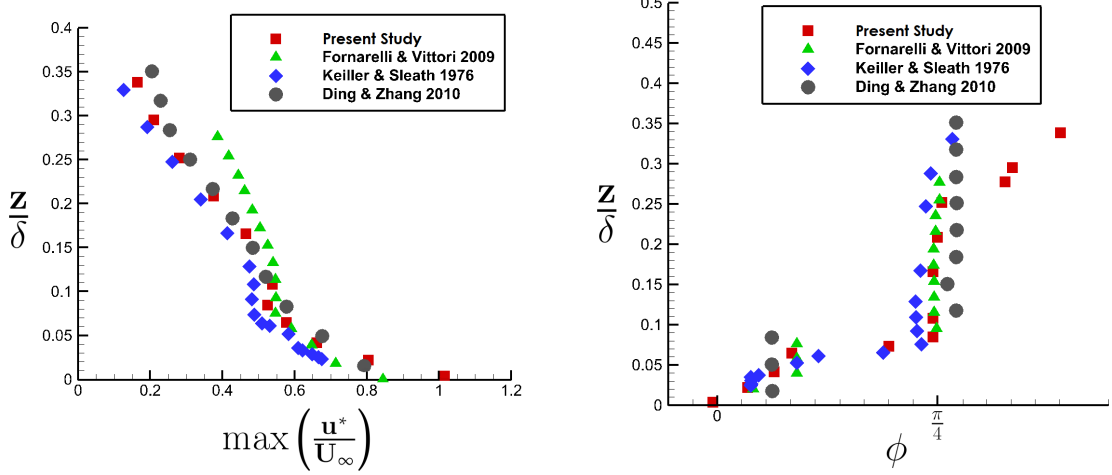
(a) Peak fluid-frame velocity vs. height above sphere crests.

(b) The phase of peak fluid-frame velocity vs. height above sphere crests.

Figure 5.2: Peak velocity phase and amplitude in the fluid frame as a function of height above the sphere crests, $Re_\delta = 95$. Note that the phases are shifted by $+\pi$ for these plots to be consistent with the notation of K&S, where $U(t) \propto -U_\infty Cos(\omega t)$.

of the hotwire anemometer beginning between $\beta z = 0.2$ and $\beta z = 0.3$ from the rough-bed surface, potentially calling into question whether the oscillations which grow approaching the wall are not simply from the growing influence of the wall on the measurement device. Also worth noting is the symmetry error apparent in this plot: To the extent that the experiment in question of K&S is an accurate representation of the geometry described, the velocity profiles should be identical from the first half cycle to the second, yet deviations on the order of 0.05δ are observed at all distances from the wall, and, at specific points, such as the $\beta z = 0.75$ probe near phases of 0 and π, they are on the order of 0.1δ. Although it is unlikely that errors in the symmetry of this experiment would induce the oscillations close to the crest or completely eliminate them far from it, it should further raise doubts about the details of their profile given that the magnitude of the oscillations is approximately the same as the errors observed between the half-cycles. It should be reiterated that the feasibility crafting appropriate boundary conditions in oscillating plate experiments for comparison with oscillating fluid flows has been called into question by [32]. Finally, the validity of a comparison by transforming a flow solution to an oscillating frame of reference is based on the approximation that the non-linear terms of the Navier-Stokes equations are negligible, which is true for a laminar Stokes flow over an oscillating flat plate, but is only an approximation for more complex sediment geometries or turbulent flows. Whether the deviations between the experiments of K&S and the simulations are a result of an under-resolved flow or particle interface in the present investigation,
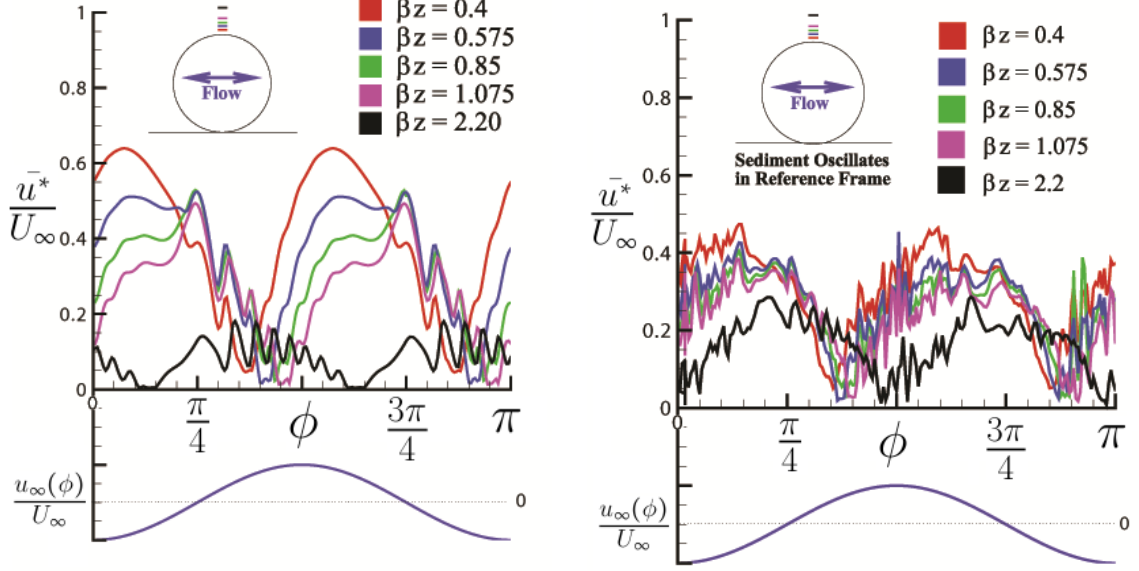
(a) Temporal fluid-frame velocity profiles of point probes above the sphere crests at $Re_\delta = 95$.

(b) Temporal fluid-frame velocity profiles of point probes above the sphere crests at $Re_\delta = 200$.

Figure 5.3: The phase-space-averaged fluid-frame streamwise velocity, $\bar{u}$, as a function of height above the sphere crests. Note that $\beta = \frac{1}{\delta}$ is adopted for consistency with K&S.

experimental error in K&S, or a breakdown of the approximation of the similarity of these flows is of relevance to the validity of the present findings and the usefulness of making such comparison. Careful observations of highly resolved simulations should be made to rule out or correct the first possibility. With the exception of these differences, the present plots describe flow characteristics similar to K&S, notably the double peak occurring at intermediate heights from $\beta z = 0.575$ to $\beta z = 1.075$. K&S showed that these secondary peaks were due to strong vertical velocities causing momentum transport from high to low-speed regions.

Figure 5.3b depicts the velocity profiles in the oscillating-fluid frame at $Re_\delta = 200$. The velocity field immediately above the crest exhibits a greater departure from a sinusoidal profile which it should approach as βz goes to 0. This is to be expected given that the increased turbulence of the higher Re_δ should impinge closer to the surface. The secondary peak and subsequent oscillations are also seen to be diminished at this Reynolds number.
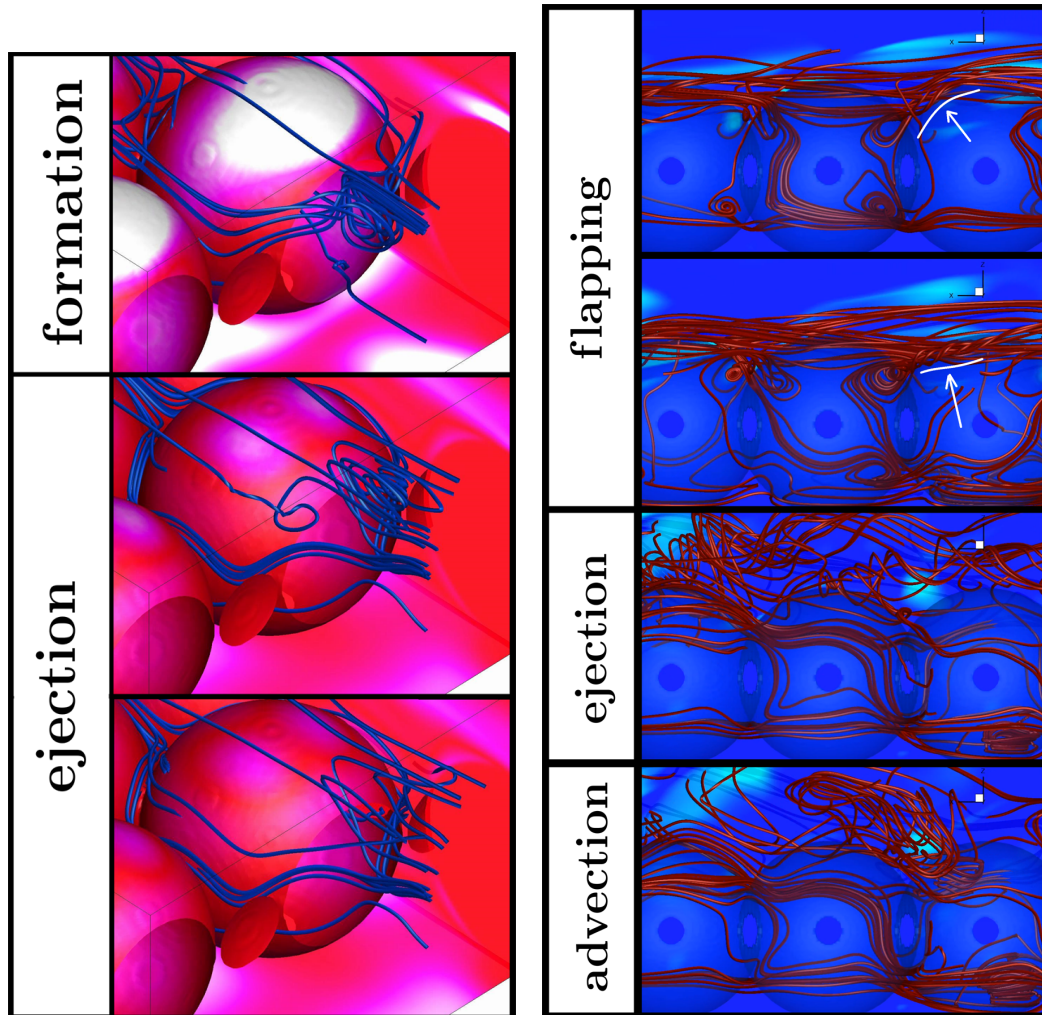
(a) At $Re_\delta = 95$, Horseshoe vortices form regularly behind sediment elements during the accelerating phase of each cycle, before being ejected at peak velocity into the surrounding fluid. This is thought to be a key mechanism in particle dislodgement [22].

(b) At $Re_\delta = 150$, the vortices can still be seen, but they periodically get pulled apart by the surrounding fluid. Later in the accelerating phase of the cycle, oscillations arise reducing the size and energy of the vortex; they are finally ejected at or shortly after peak velocity.

Figure 5.4: Comparison of coherent vortex structures by means of streamlines at $Re_\delta = 95$ and 150. Note that while all of these images are in order and from the same sphere, period, and flow, they are not evenly spaced, but rather, are intended to convey the general trends of the cycle throughout the accelerating phase until shortly after the peak velocity, when the flow becomes especially chaotic.
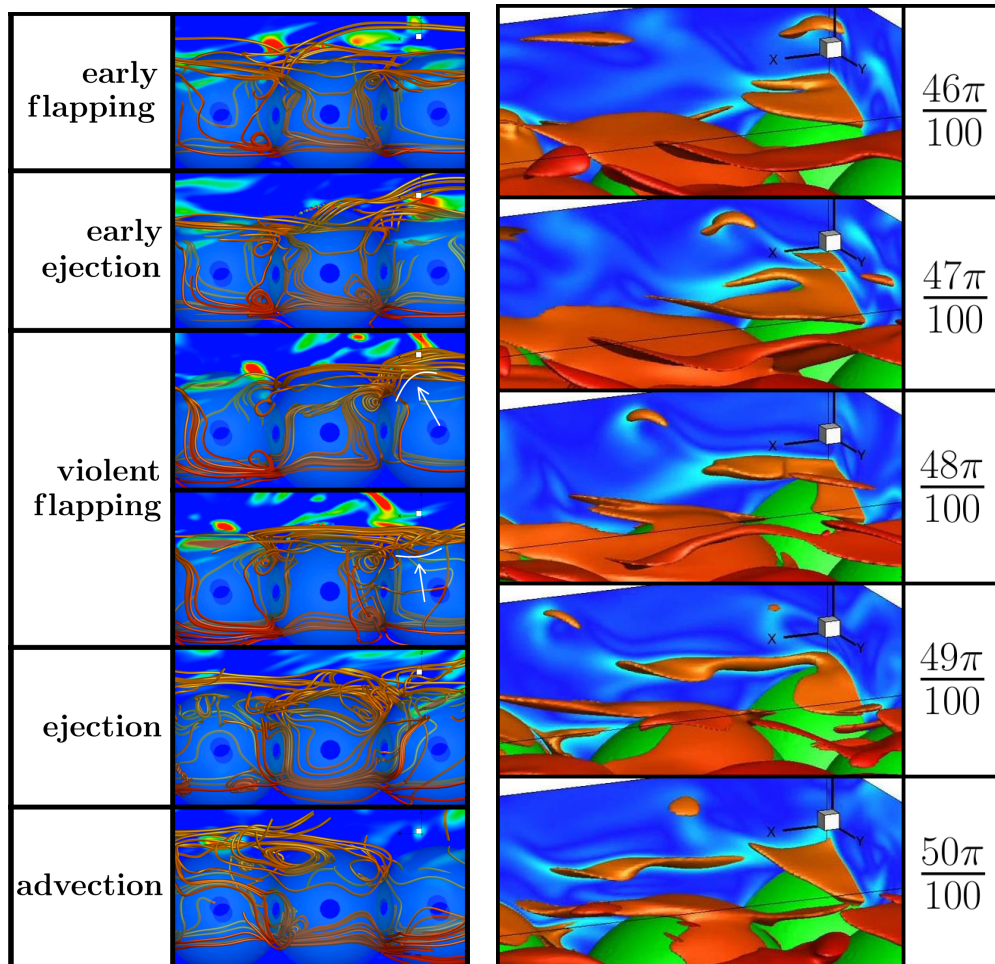
(a) The $Re_\delta = 200$ case features early oscillations and minor ejections of the vortex, followed by violent vertical flapping of the tails of the vortex, which wrap around individual spheres and elongate in the flow. These are finally ejected in a manner that is less distinct in time than the $Re_\delta = 150$ case.

(b) Isosurfaces of vorticity are used at $Re_\delta = 200$ to clearly depict the flapping oscillations which characterize the flow and seem to have a consistent frequency.

Figure 5.5: Comparison of coherent vortex structures by means of streamlines at $Re_\delta = 200$. Note that while all of these images are in order and from the same sphere, period, and flow, they are not evenly spaced, but rather, are intended to convey the general trends of the cycle throughout the accelerating phase until shortly after the peak velocity, when the flow becomes especially chaotic.

5.2   Evolution of Vortex Structures

Fornarelli and Vittori (2009) [22] noted the existence of horseshoe-shaped vortices in their $Re_\delta = 95$ case. These formed behind the spheres during the accelerating phases of the cycle and were released into the fluid around the peak velocity. Despite changes in geometry and turbulence, the present $Re_\delta = 95$ case also featured these vortical structures, which are shown in figure 5.4a. These structures are likely responsible for the "secondary peak" which received much attention in Keiller and Sleath's 1975 study on this topic [30]. The ejection of these structures coincide with the peak lift experienced by the particles, and so it is likely that they are instrumental in particle erosion in this parameter range.

Observations of videos of line probes at $Re_\delta = 150$ (figure 5.4b), indicate that the horseshoe vortices, which were present and totally regular at $Re_\delta = 95$, stretch out and experience vertical flapping with opposite ends out of phase. This behavior gets increasingly energetic until shortly after the peak velocity at $\phi = \frac{\pi}{2}$ when the vortex leaves the sphere with less energy compared to the punctuated symmetrical ejections at $Re_\delta = 95$. The $Re_\delta = 200$ case features flapping earlier on in the cycle as well as (at least one) noticeable early ejection of all of the vortex structure (figure 5.5a). The flapping becomes violent around peak bed velocities, and the vortices continue to form even after a strong ejection has occurred at the peak velocity, so there is no longer a clear, single ejection event. Based on observations of this trend, it is expected that the ejection of the vortices, and therefore the vortices themselves, will have a diminished impact on the flow at higher Reynolds numbers. Of course, if $\frac{D}{\delta}$ decreases, as it would for realistic coastal parameter ranges, then ejection events could remain important even at higher Re_δ due to the vortex structures on the scale of the particles being smaller compared to the scales of viscous dissipation; as of yet, it's unclear exactly how the flow will respond to smaller particle sizes. Figure 5.5b depicts the flapping more clearly than is apparent from streamlines via isosurface contours of vorticity leading up to the peak velocity at $\phi = \frac{\pi}{2}$.

Vertical profiles of the phase-space-averaged streamwise velocity at different points relative to the spheres are depicted in figures 5.7, 5.8, and 5.9. These are analogous to figure 11 of F&V; however, their line probes cannot be located with certainty due to an erroneous depiction of the flow direction in their particle guide, figure 10. See figure 5.6 for the positions of these probes relative to the sphere for this study. Because the spheres are not in contact with one another in the simulations of F&V, the flow at probe B, which is in the trough between the spheres, is not constrained as it is in the present case. Their case is also turbulent at $Re_\delta = 95$ due to the sediment spacing, as has been discussed. Finally, note that the phases included in the figures presented here are staggered in between those depicted in figured 9 of F&V. The use of phases $\phi = 0$ and $\phi = \frac{\pi}{2}$ for the line
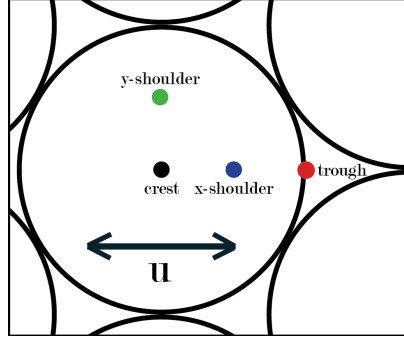
Figure 5.6: Locations of the line probes relative to the sediment elements used in figures 5.7, 5.8, 5.9, 5.10, 5.11, and 5.12.

probes in figures 5.7, 5.8, and 5.9 implies that $\frac{u(z)}{U_\infty}$ should approach 0 and 1 at large z, respectively. $u_\infty(\frac{\pi}{4})$ will be equal to $u_\infty(\frac{3\pi}{4})$, highlighting the hysteresis due to the presence of the bed. These advantages come at the expense of missing the inflection points of the profiles found in figure 11a at $\phi = \frac{13\pi}{8}$ of F&V, which is likely due to vortex ejection occurring at that phase and Reynolds number, as well as the moment of flow reversal of the bed velocity in figure 11b at $\phi = \frac{15\pi}{8}$ (note that phases in F&V have a $\frac{\pi}{2}$ lead over the system used here). The information presented in figure 11 of F&V is in general agreement with the data presented here in figure 5.7.

Looking at the line probes of the streamwise velocity found in figures 5.7, 5.8, and 5.9, the vertical extent of deviations in the velocity profiles from $u_\infty(\phi)$ increases with the Reynolds number, approaching the far-stream profile at approximately $a = 11$, 15, and 18 respectively. This might be explained by the increasing development of turbulence causing greater momentum exchange than it did in the laminar regime at $Re_\delta = 95$; it will not continue to increase with Re_δ if $\frac{D}{\delta}$ is held constant as the boundary layer thickness $\delta = \sqrt{\frac{2\nu}{\omega}}$ is independent of velocity and particle diameter (see equation 2.4). The trough probes in figures 5.7d, 5.8d, and 5.9d illustrate the extent of the phase lag in the pore space (see figure 5.21 for quantification of this); however, it also highlights the degree to which the phase lag on this probe is approximately the same above and below the sphere centerline.

Figures 5.8c and 5.8d at $Re_\delta = 150$ and 5.9b, 5.9c, and 5.9d at $Re_\delta = 200$ all indicate a quadruple inflection in $\bar{u}$ between $z = 7$ and 10. These may just be artifacts of fluctuations that have failed to average out given the sample size (16 for $Re_\delta = 150$ and 40 for $Re_\delta = 200$); however the flapping behavior seen at these Reynolds numbers in the time lapse of vorticity isosurfaces and streamlines may be responsible for producing the quadruple inflection, that is, it is possible that the flapping behavior yields two regions which attract flow with unstable feedback, resulting in increased veloc-

ities in these two regions more so than the flow between them. Furthermore, $\bar{u}$ above the crest in figure 5.9b at $Re_\delta = 200$ has a double inflection which likely corresponds to an earlier, smaller vortex ejection occurring during the accelerating phase of the cycle, which is not present at lower Reynolds numbers. This hints at the possibility that ejected structures may continue to play an important role at higher Reynolds numbers; the peak lift on the particles leads the bed velocity in phase (figure 5.13, discussion at the end of section 5.2), meaning that these structures, if ejected earlier during the accelerating phase, may be striking at just the right moment to dislodge a particle near the critical Shields parameter.

As lift is primarily responsible for the ejection of embedded particles and is commonly modeled in relation to the dynamic pressure acting over the particle surface via the velocity squared, that is $C_L \propto u_b^2$, where u_b is the bed velocity located in the log layer immediately above the effective bed location, $\bar{C}_L$ and $\bar{u}_b^2$ are plotted in figures 5.13a, 5.13b, and 5.13c at $Re_\delta = 95$, 150, and 200 respectively. Here, C_L is computed with respect to U_∞, making it a non-dimensional form of the lift force. The $Re_\delta = 95$ case features an early peak that is not present in figure 17 of F&V. Note that for the purposes of this investigation, u_b is defined as the streamwise component of the velocity above the sphere crest as opposed to the magnitude of the velocity. The impact of vortex ejection, suspected of causing the secondary peaks apparent in figure 5.3a and figure 2 in K&S [30], ought to effect the lift a quarter cycle later where no distinct perturbation is noted. This suggests that vortex ejection has a minimal impact on particle lift and that some other flow mechanism, thus far unobserved, is responsible for the early fluctuation. The lift is found to lead the bed-flow velocity by approximately $30°$ at $Re_\delta = 95$, in agreement with F&V, although this lead was found to diminish with increasing Reynolds numbers. The phase lead of the lift can be attributed the phase lead of the pore-space velocity pulling down on the sphere at reversal of the bed-flow velocity (see section 5.4). The diminishing of this lead at higher Re_δ is not due to a diminishing of the phase lead in pore space (see figure 5.21), but to a diminishing relative magnitude of pore-space velocity near bed-velocity reversal.

Figures 5.10, 5.11, and 5.12 depict the vertical profiles of the mean turbulent kinetic energy at the probes from figure 5.6. TKE's at $Re_\delta = 95$, as shown in figure 5.10, highlight the lack of turbulence at these parameters and reinforce the notion that the flow simulation features natural disturbances which would trigger turbulence in the appropriate parameter ranges, but that these perturbations are damping out at $Re_\delta = 95$, unlike the case of F&V. At $Re_\delta = 150$ and $Re_\delta = 200$, the double peaks above the crest are likely an indicator of the same phenomenon that is responsible for quadruple einflection of the $\bar{u}$ probes, possibly a result of the flapping motion of the ejected vortices. One oddity is the clear double peak shown at the X-shoulder probe at $\phi = 0$. At this phase, the fluid should have ejected all vortices formed behind sphere, which would have advected well beyond the shoulder of the same sphere given the relative magnitude of the free-stream velocities to

the particle diameters. Perhaps there are frequent vortices advecting at consistent heights from the spheres over multiple domain-lengths. The turbulent kinetic energy is highest relative to the mean flow for $Re_\delta = 150$ (figure 5.11). The decreasing trend is expected to continue into higher Reynolds numbers; just like the lift coefficient was expected to peak at intermediate Reynolds numbers as discussed in F&V and K&S, the TKE, related to the square of the velocity, will probably decrease into higher Re_δ's. The TKE is seen to be significant in the trough between the center and crest of the sphere at $Re_\delta = 200$ at $\phi = \frac{\pi}{2}$ but not $Re_\delta = 150$ (figure 5.12c).

The line probes of $Re_\delta = 200$ also indicate a slight source of error in that simulation as the velocities do not appear to converge to zero at $\phi = 0$ as $z \to \infty$. The source of error is unknown, but it is almost certainly not part of the correct flow. The analytical flat-plate solution requires the velocity to exponentially decay with $e^{\frac{z}{\delta}}$, which is not happening in figure 5.9a [54]. The source of this error is unknown; one possibility is that a few erroneous data points of nonzero velocity got mixed into the set. Another problem, which is not apparent from the line probes, is that the data from one cycle to the next in the $Re_\delta = 200$ case (on eight different spheres) tends to be clustered together compared to the entire set of values, which is a clear sign that the domain is too small and that the solution is not an instantaneous representation of an infinite extent of spheres; however, the phase-space-averaged statistics still may be an accurate representation of the flow. It is difficult to confirm this without larger and longer simulations to compare it with.

5.3   Probability Distribution Functions of Turbulent Properties

The stochastic properties of turbulence have been investigated for the $Re_\delta = 200$ case exclusively. As has been hypothesized in section 2.3, non-Gaussian u_b' fluctuations were expected to be observed in regions of rapid local increase of turbulent kinetic energy. Figures 5.12b and 5.12c indicate that this is happening directly above the sphere at phases from the middle of the accelerating cycle to peak velocity. At these phases, the local bed velocity leads $u_\infty(\phi)$ significantly (see figures 5.7b, 5.8b, and 5.9b). In the present study, probability distribution functions of the bed-fluid parameters are attained by sampling a region of fluid on a line probe immediately above the crest of the spheres. The sampling range was fixed between $7.05\delta < z < 8.05\delta$ or 0.1δ to 1.1δ above the sphere crest. This range was chosen as a sample of the instantaneous log layer of flow; however the crest line probes of u_b in figures 5.7d, 5.8d, and 5.9d as well as figure 5.7a experience a flow reversal within δ of the sphere crest. This poses a challenge for correlating the local bed velocity, u_b, to the forces acting on the particles as the turbulence in the selected sampling region above the crest may not reflect that of the instantaneous log layer. For future simulations, it will be desirable to sample velocities over a smaller range of heights above the sphere and over a broader region in the streamwise and spanwise

(a) $\phi = 0$ (b) $\phi = 0.125$ (c) $\phi = 0.25$ (d) $\phi = 0.375$

Figure 5.7: Vertical $\bar{u}_x$ profiles at different points above the spheres at $Re_\delta = 95$, indicated by figure 5.6.

(a) $\phi = 0$ (b) $\phi = 0.125$ (c) $\phi = 0.25$ (d) $\phi = 0.375$

Figure 5.8: Vertical $\bar{u}_x$ profiles at different points above the spheres at $Re_\delta = 150$, indicated by figure 5.6.

Figure 5.9: Vertical $\bar{u_x}$ profiles at different points above the spheres at $Re_\delta = 200$, indicated by figure 5.6.

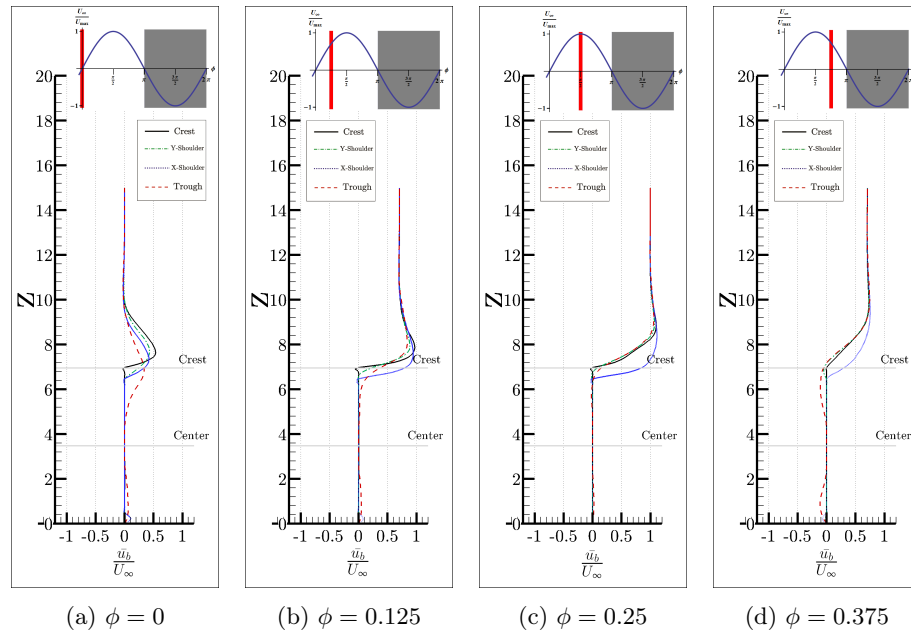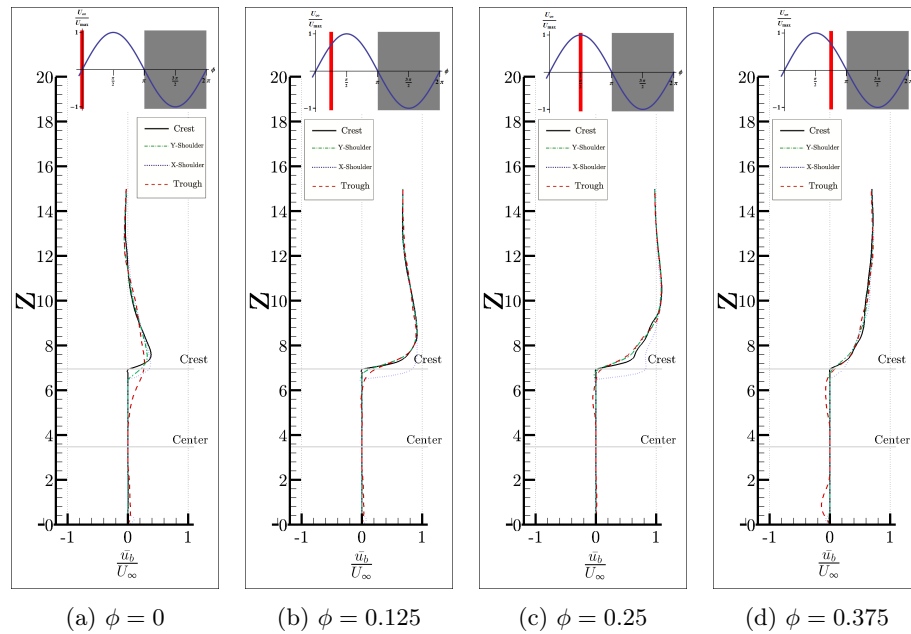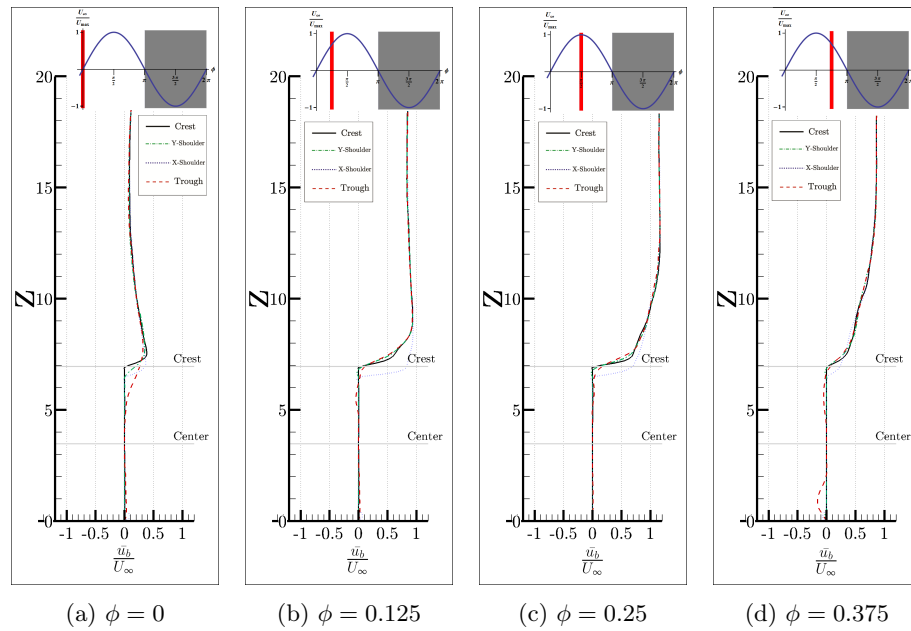
Figure 5.10: Vertical $T\bar{K}E$ profiles at different points above the spheres at $Re_\delta = 95$, indicated by figure 5.6.

Figure 5.11: Vertical $T\bar{K}E$ profiles at different points above the spheres at $Re_\delta = 150$, indicated by figure 5.6.

direction (to increase the sample size). For the purposes of this thesis, the most important phase is near peak lift, and therefore potential ejection, and will still have a bed-velocity sampled within the instantaneous log-layer. It is possible that the use of an instantaneous log layer for this purpose is not necessary as the particle forces will be a reflection of the complex dynamics of the flow in its immediate vicinity regardless of its profile.

Flow samples were sorted into ten bins per half cycle. In order to maximize the sample size of the bed-flow turbulence, statistics from the back half of the cycle were combined with the front half. Fluctuations of properties which are dependent on the sign of the flow, such as u_b, $u_b |u_b|$, and C_D were multiplied by -1, while flow properties such as u^2 and C_L were used as they were. Even with this added data, typical sample sizes of the bed-flow properties did not exceed 10000 per $18°$ sampling period.

Based on the profiles depicted in figure 5.12, the TKE is observed to increase substantially between $\phi = \frac{\pi}{4}$ and $\phi = \frac{\pi}{2}$ above the surface of the spheres at $Re_\delta = 200$. A significant decrease in TKE is observed a quarter cycle later; based on these ranges, turbulence samples of u_b' from phases of $\frac{3\pi}{10} < \phi < \frac{4\pi}{10}$ and $\frac{8\pi}{10} < \phi < \frac{9\pi}{10}$ have been selected to compare the distributions. Skewed

(a) $\phi = 0$ (b) $\phi = 0.125$ (c) $\phi = 0.25$

(d) $\phi = 0.375$

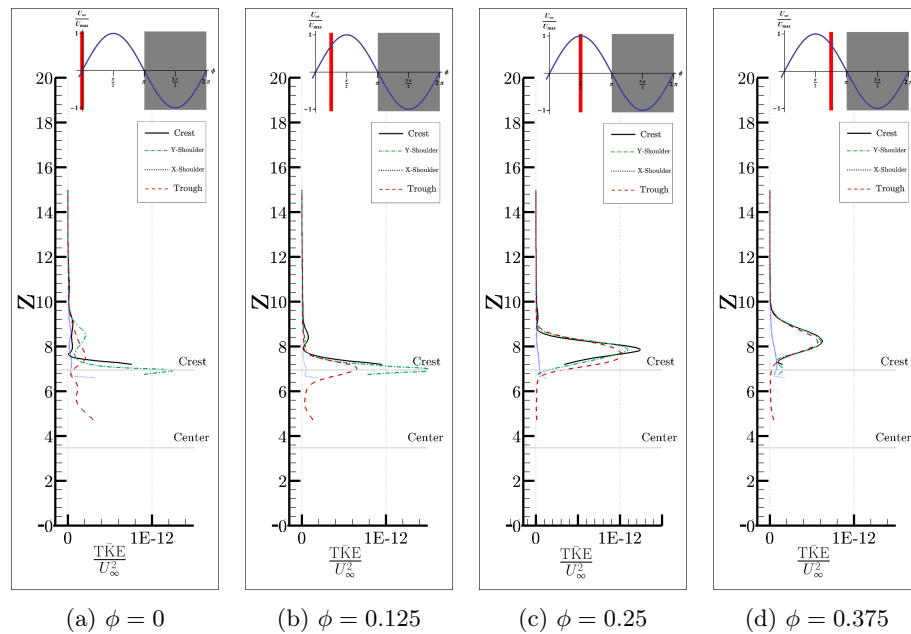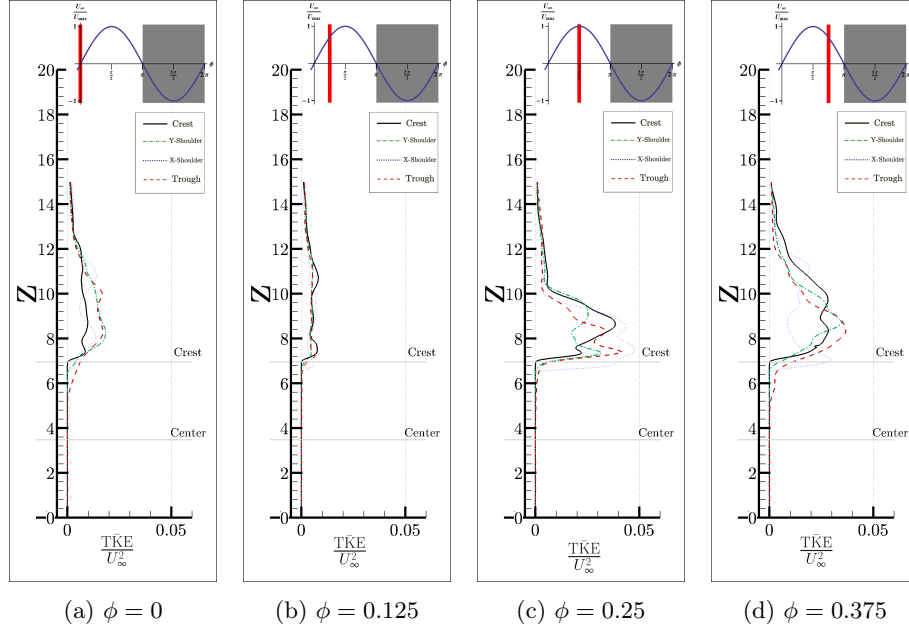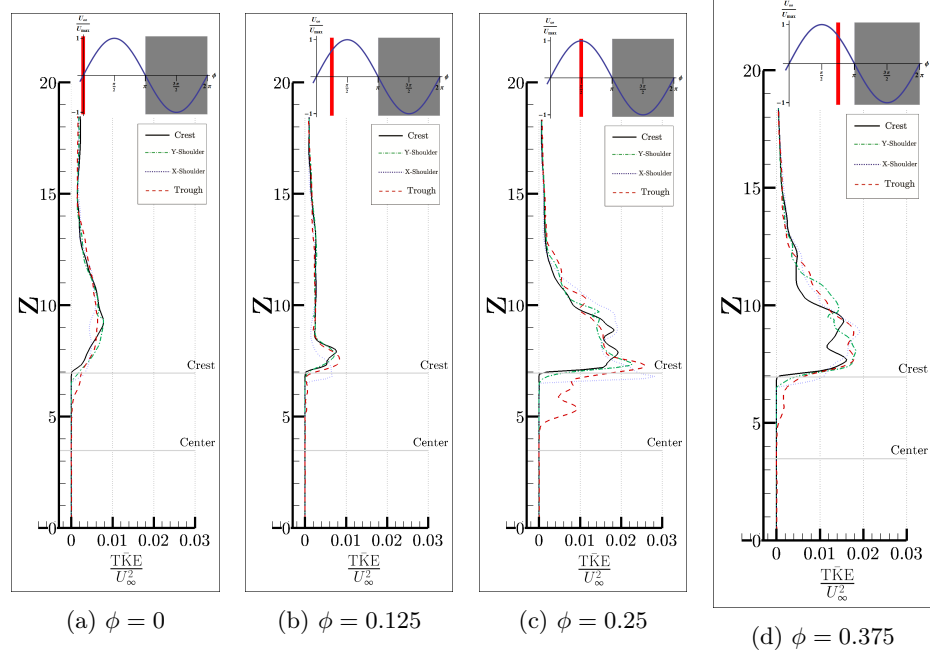Figure 5.12: Vertical $T\bar{K}E$ profiles at different points above the spheres at $Re_\delta = 200$, indicated by figure 5.6.

(a) $Re_\delta = 95$ (b) $Re_\delta = 150$ (c) $Re_\delta = 200$
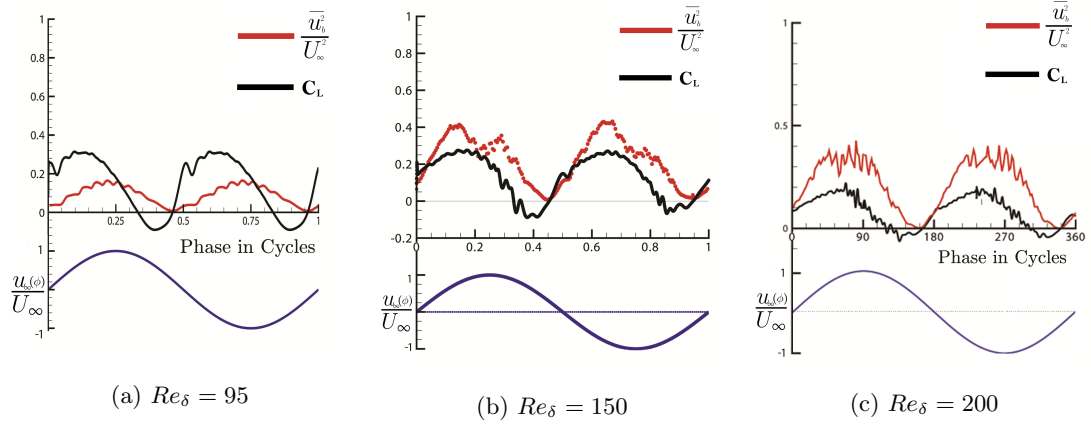
Figure 5.13: The phase-space-averaged lift coefficient, $C_L = \frac{F_L}{\frac{1}{2}\rho_{fl}U_\infty^2 A}$, evolutions over the cycle compared with $\frac{\bar{u_b^2}}{U_\infty^2}$ for different Reynolds numbers.

distributions resulting from local surface-related instabilities generating turbulent kinetic energy are depicted in figures 5.14a, while the expected symmetrical distributions resulting from non-local turbulence dissipation are displayed in figure 5.14b. This, in agreement with the predictions of section 2.1, suggests that assumptions of Gaussian distributions of the bed velocity are not instantaneously accurate and should not be used as the basis of theoretical derivations of forcing distributions as a function of phase as is commonly done in steady flows.

Given that it is the aim of this investigation to develop improved stochastic sediment transport models, and that such models are often (and most successfully) built via relations of F_L and F_D to the bed velocity (see equations 2.2 and 2.3), it is of interest to see how PDFs of $u_b^{2'}$ compares to those of F_L'. The lift is chosen in favor of the drag due to its relative importance in dislodging embedded particles. Figures 5.15 and 5.16 show PDFs of $u_b^{2'}$ and C_L', respectively, at $Re_\delta = 200$. In this case, C_L is defined with respect to the maximum velocity far from the bed, U_∞, and is thus a non-dimensional measure of the instantaneous lift force, F_L. The PDFs of $u_b^{2'}$ exhibit positive skewness during the accelerating phase of the cycle and briefly Gaussian behavior at $\phi = \frac{15\pi}{20}$, before compressing into highly peaked distributions at $\phi = \frac{17\pi}{20}$ and $\frac{19\pi}{20}$ (figures 5.15i and 5.15j). It is not clear from visual inspection whether these trends are reflected in the lift PDFs. Focusing on the phases investigated for the u_b' distributions, in can be seen that at $\frac{3\pi}{10} < \phi < \frac{4\pi}{10}$, $u_b^{2'}$ features a similar distribution to u_b' in figure 5.14a; however, the PDF of lift at this phase does not reflect the bed velocity intensity and actually has a skewness of opposite sign. The PDF of $u_b^{2'}$ at $\frac{8\pi}{10} < \phi < \frac{9\pi}{10}$ is much more peaked than that of u_b' in this phase range. The lift fluctuations in this sampling range, C_L', can be seen to be peaked, although not nearly to the extent of $u_b^{2'}$.

While a straightforward correspondence between the PDF's of the fluctuations in the bed velocity intensity and lift coefficient C_L were not demonstrated, the observations can be explained. PDFs of $u_b^{2'}$ can only be expected to be similar to those of u_b' if the relative turbulence intensity, $\frac{\sigma_{u_b}}{\mu_{u_b}}$ goes to 0, as discussed by [26] and in section 2.1, otherwise, the PDF is significantly transformed. In the case of a Gaussian PDF of u_b, the PDF of u_b^2 should become a non-central χ^2 distribution which is more peaked and skewed. The fluctuating component, $u_b^{2'}$ will follow these trends. Figure 5.18a displays the velocity in the center of the range $\frac{8\pi}{10} < \phi < \frac{9\pi}{10}$, corresponding to the highly peaked PDF of the bed velocity intensity in figure 5.15i; flow reversal immediately at the crest can be seen to occur at or immediately after this sample. At this moment, the mean bed velocity goes to zero while turbulence is still present (see the TKE in figure 5.18b). Thus, it is not surprising that in the sampling range of this PDF, the relative turbulence intensity of 1.2 results in a more peaked distribution of u_b^2 and, therefore, of $u_b^{2'}$. The PDF of u_b^2 is fit with χ^2 and log-normal distributions in figure 5.17. This plot shows better agreement between the χ^2 fit and the data than the Gaussian distribution in figure 5.15i. It is possible that some error may have been introduced at this phase due to the reversal

of the fluid immediately above the sphere: the instantaneous region of linear velocity profile may expand to above 0.1δ above the sphere crest, where the bed velocity is computed; however, resizing the sampling height failed to significantly reduce the kurtosis at that phase.

The skewness and kurtosis of the PDFs of $u_b^{2\prime}$ and $C_L^\prime$ are plotted as a function of phase in figure 5.19. These moments indicate a weak correlation in a few parts of the cycle, namely, the signs and approximate magnitude of the changes in skewness at phases from $\frac{19\pi}{20} < \phi < \frac{\pi}{4}$ as well as the values of kurtosis in the range of $\frac{7\pi}{20} < \phi < \frac{3\pi}{4}$. The skewnesses of $C_L^\prime$ and $u_b^{2\prime}$ are, however, of opposite signs of one another for significant portions of the cycle. A large peak in kurtosis and skewness occurs in the PDF of $u_b^{2\prime}$, which is the phase discussed in detail due to its high relative turbulence intensity at local flow reversal. If the fluctuations in lift were a reflection of the fluctuations occurring in the bed velocity intensity (and therefore pressure) immediately above the sphere crest, the higher moments of the lift fluctuations would also reflect those of the $u_b^{2\prime}$ distribution. The poor quality of correlations shown in figure 5.19 demonstrates that this is not the case. This can be explained by the rigid particle acting as a low-pass filter, smoothing out low wavenumber fluctuations occurring over its surface and possibly reducing the extremity of the higher moments of its fluctuations. It is also likely that the fluctuating velocity intensity is characterized by different distributions at different points around the surface of the sphere, so the bed-velocity should be sampled from a wider region than immediately above the crests. The vertical and spanwise components of velocity are also likely relevant in the resulting lift fluctuation, so the bed velocity should be defined as the sum of all three components for better results: $u_{b,better}^2 = u_x^2 + u_y^2 + u_z^2$.

Again, a straightforward correspondence between the fluctuations of u_b^2 and C_L was not observed in the higher moments of the PDFs displayed in figure 5.19; however, the many discrepancies may be explained by a failure to properly sample the bed velocity and to account for natural spatial filtration of high-wavenumber velocity fluctuations. The kurtosis of the bed velocity intensity fluctuations appears to be correlated with the lift fluctuations near peak velocity, where the relative turbulence intensity is smallest and the intensity of flow is dominated by the intensity of the x-component of velocity (the bed-velocity). This suggests the peaked distribution occurring at flow reversal above the sphere crest may be highly localized and washed out by relatively normal distributions occurring on the shoulders of the sphere and even beneath the sphere. In general, the possibility of relating the PDF moments of the velocities in the flow to those of the lift force still appears attainable if the suggested issues are addressed.
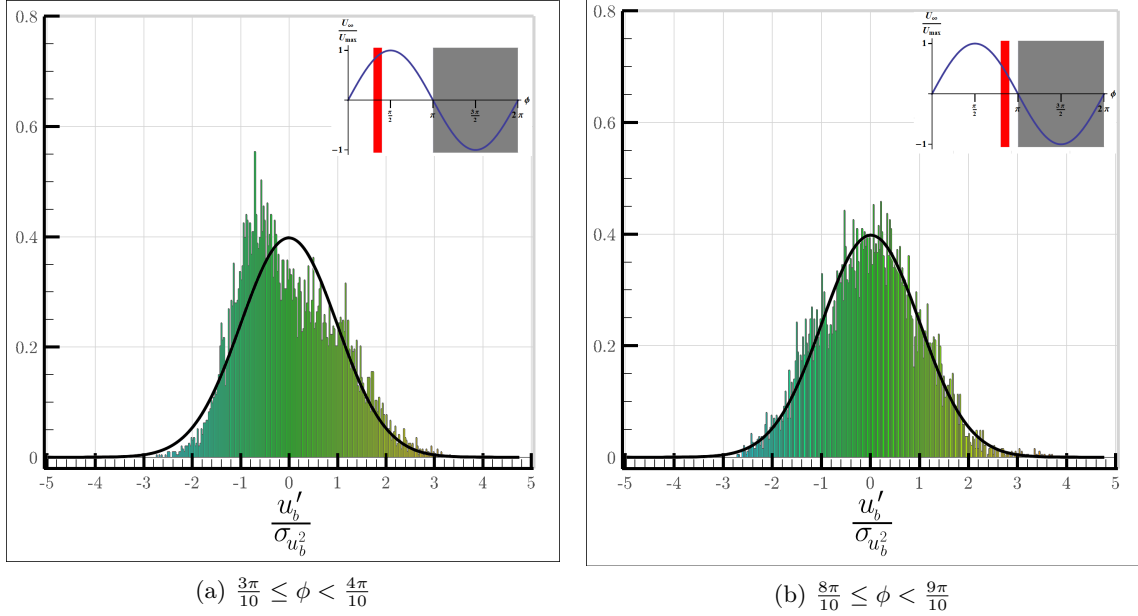
(a) $\frac{3\pi}{10} \le \phi < \frac{4\pi}{10}$　　　　(b) $\frac{8\pi}{10} \le \phi < \frac{9\pi}{10}$

Figure 5.14: The PDF of u_b at $Re_\delta = 200$. The bed velocity is taken to be the region directly above the crest of the sphere in the range $7.05\delta < z < 8.05\delta$ or 0.1δ to 1.1δ above the crest. The inclusion of a gap of 0.1δ eliminates the instantaneous linear boundary-layer region, which otherwise produces and excessively peaky distribution.

5.4   Pore Space Flow Properties

Understanding the phase lag and turbulence properties of the pore space will be necessary for accurate modeling of the lift force distribution across realistic parameters ranges of coastal flow. For instance, if the pore-space velocity (equation 5.2) peaks later in the cycle at more energetic parameter ranges than it does here, it will serve to reduce the net lift on the sphere when it is at its peak, which would reduce the chances of ejection. This is because the moving fluid pulls down on the sediment from below, as demonstrated in the brief period of negative lift preceding flow reversal in figure 5.13c. At the same time, if the absolute size of the turbulent fluctuations in the pore space becomes significant compared to the magnitude of the lift, the PDF of the turbulent properties in the pore space will need to be known to predict the overall PDF of the lift on the sediment and the probability of its ejection. The phase of flow reversal in the pore space and bed velocity are shown in figure 5.21, which indicates little appreciable change in phase lag at these parameters; however, the pore-space flow is not yet turbulent in any of the present simulations. Based on velocity profiles found at line probes to the side of the spheres in the spanwise direction of the $Re_\delta = 200$ case, the pore Reynolds number, Re_p, defined in equation 5.1, can be estimated to be in the range of
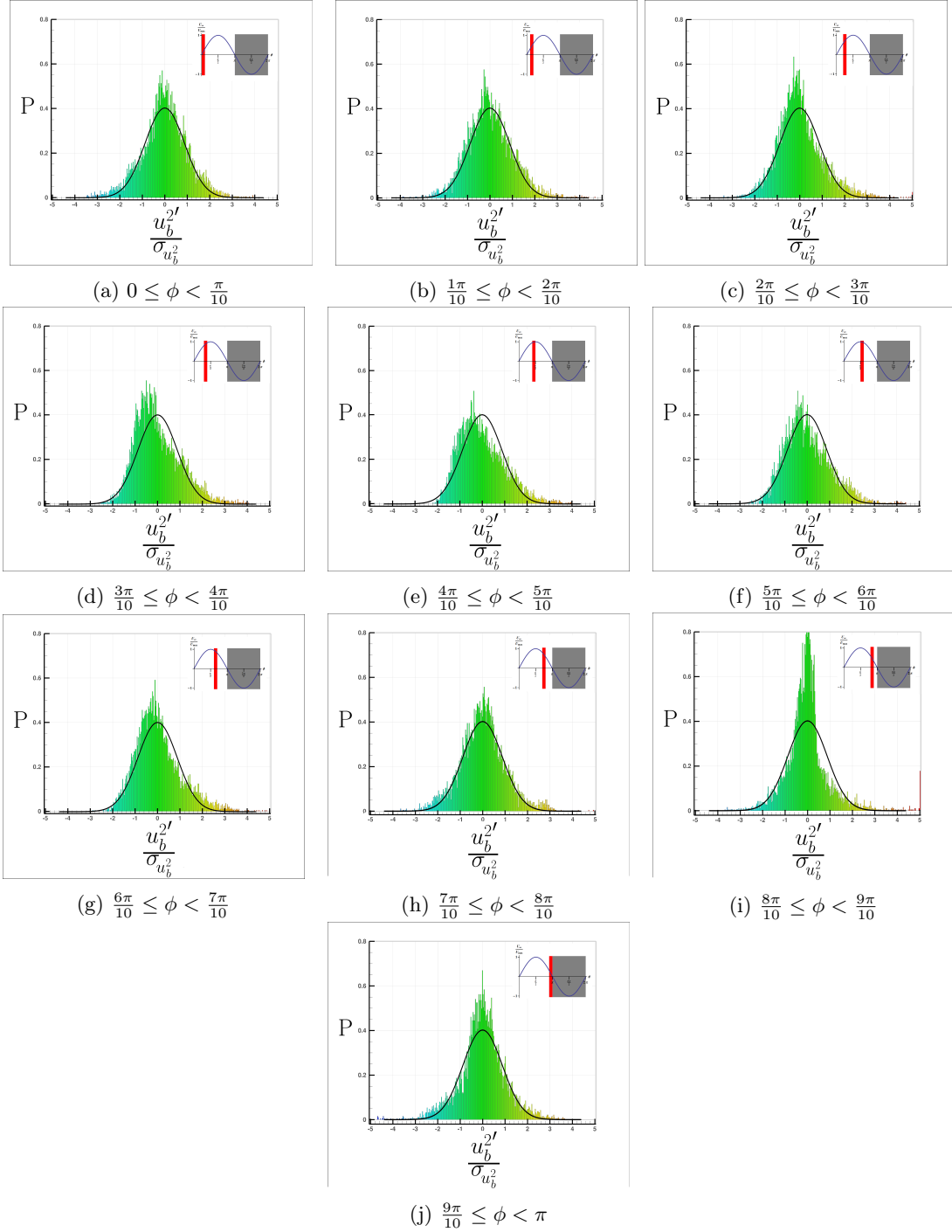
Figure 5.15: PDFs of $u_b^{2\prime}$ at $Re_\delta = 200$. As with the $u_b^\prime$ distribution in figure 5.14, the bed velocity is taken to be the region directly above the crest of the sphere in the range $7.05\delta < z < 8.05\delta$ or 0.1δ to 1.1δ above the crest. The inclusion of a gap of 0.1δ eliminates the instantaneous linear boundary-layer region, which otherwise produces and excessively peaky distribution.

(a) $0 \leq \phi < \frac{\pi}{10}$

(b) $\frac{1\pi}{10} \leq \phi < \frac{2\pi}{10}$

(c) $\frac{2\pi}{10} \leq \phi < \frac{3\pi}{10}$

(d) $\frac{3\pi}{10} \leq \phi < \frac{4\pi}{10}$

(e) $\frac{4\pi}{10} \leq \phi < \frac{4\pi}{10}$

(f) $\frac{5\pi}{10} \leq \phi < \frac{6\pi}{10}$

(g) $\frac{6\pi}{10} \leq \phi < \frac{7\pi}{10}$

(h) $\frac{7\pi}{10} \leq \phi < \frac{8\pi}{10}$

(i) $\frac{8\pi}{10} \leq \phi < \frac{9\pi}{10}$

(j) $\frac{9\pi}{10} \leq \phi < \pi$
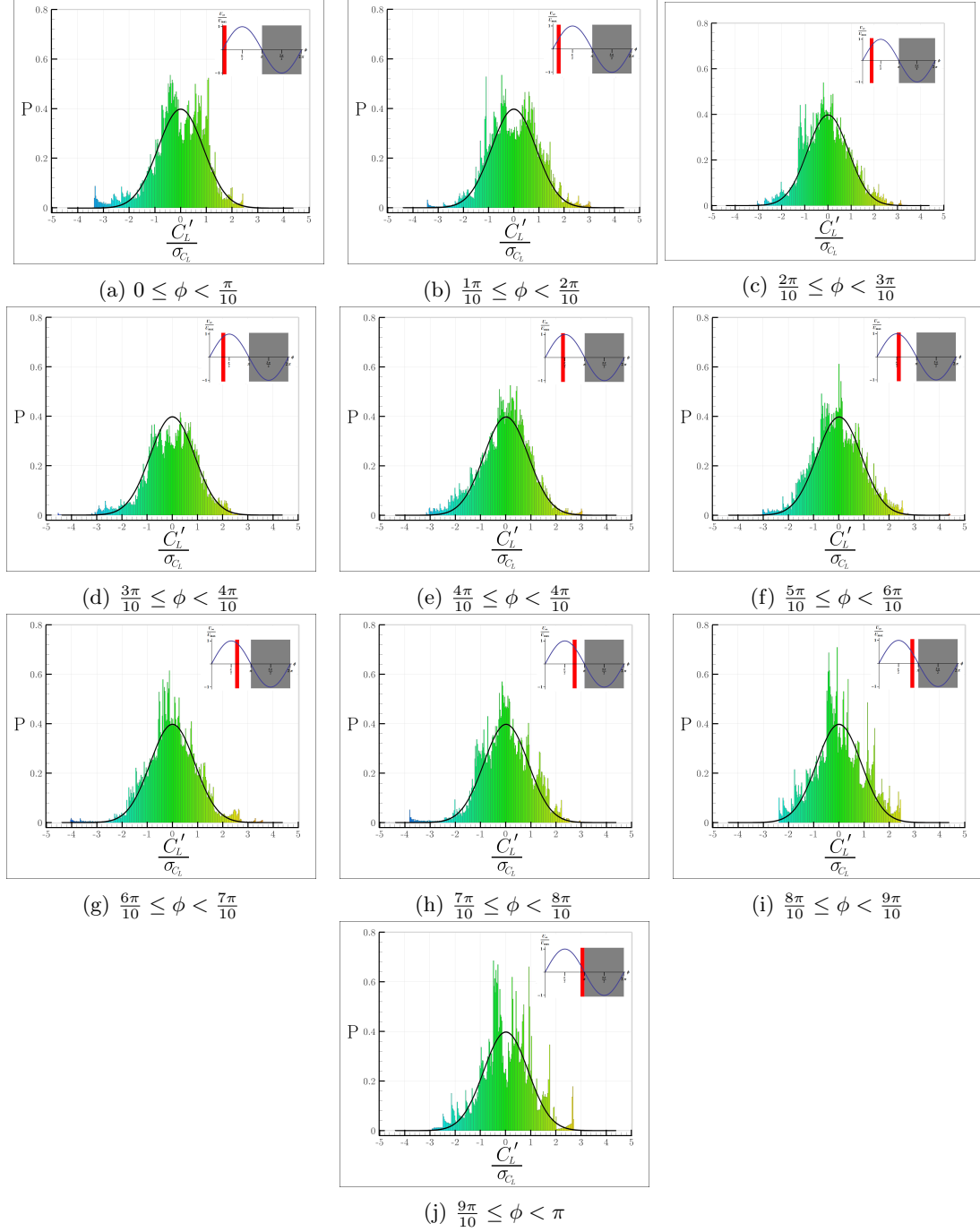
Figure 5.16: PDFs of C_L' at $Re_\delta = 200$.

Figure 5.17: The probability distribution function of instantaneous u_b^2 (not the fluctuating component) at $\frac{8\pi}{10} \leq \phi < \frac{9\pi}{10}$ at $Re_\delta = 200$. This corresponds to the highly peaked distribution of the fluctuating component of the u_b^2 in figure 5.15i. The discrete distribution is then fitted with appropriate χ^2 and log-normal continuous distributions. The inverse of the relative turbulence intensity was used to determine the appropriate non-centrality parameter of the χ^2 distr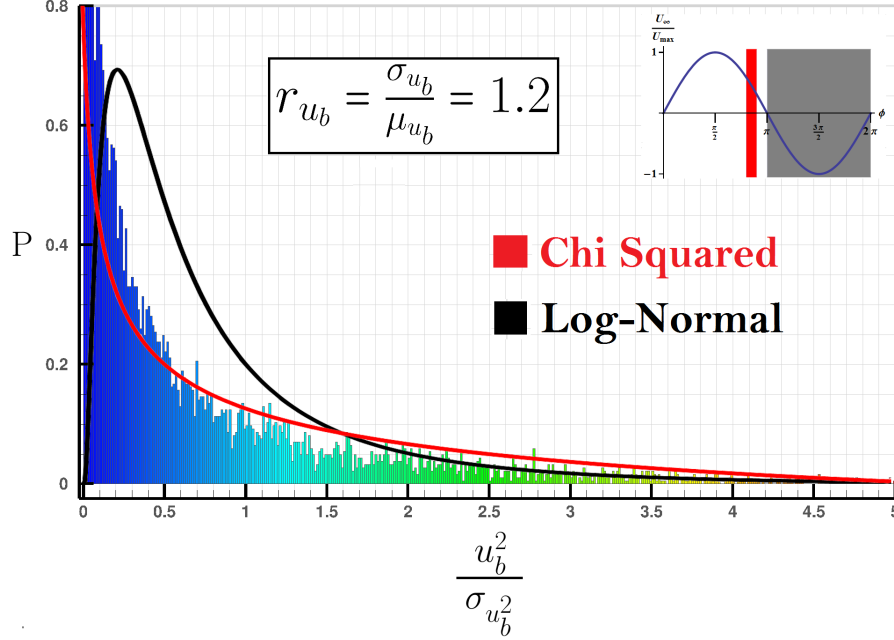ibution, as suggested by [26], which is 1.2 in this sample when determined with respect to the bed velocity in the boundary layer thickness directly above the sphere crests, $7.05 < \frac{z}{\delta} < 8.05$. The log-normal distribution was fit directly with the mean and standard deviations of the bed-velocity intensity during the phase sample. The validity of this fit was suggested by [39] to be a function of the 2-point correlation length of the velocities, which were not measured for this sample.

$50 < Re_p < 100$ at peak velocity, which is well below the approximate threshold to full turbulence in steady porous flows described by Horton and Pokrajac (2009) [27] of $Re_p = 300$ for regular packing configurations. If the present simulations were to feature an additional layer of stacked spheres beneath the surface layer, the pore space flow might be affected. If a hexagonal pattern were used and stacked in a staggered manner, the pore-space flow would feature a more consistent channel diameter, but would not have a much larger Re_p; however, if an orthogonal pattern of spheres were used, as done by D&Z [16], the d_p would approximately double, and Re_p would increase by $\mathcal{O}(d^2) = \mathcal{O}(4)$, in addition to aligning the channels, potentially resulting in turbulent flow around $Re_p = 300$, or otherwise disturbed laminar flow, as opposed to the linear laminar flow of the present study. This is, of course, assuming that the steady flow model will provide a useful estimate of the instantaneous

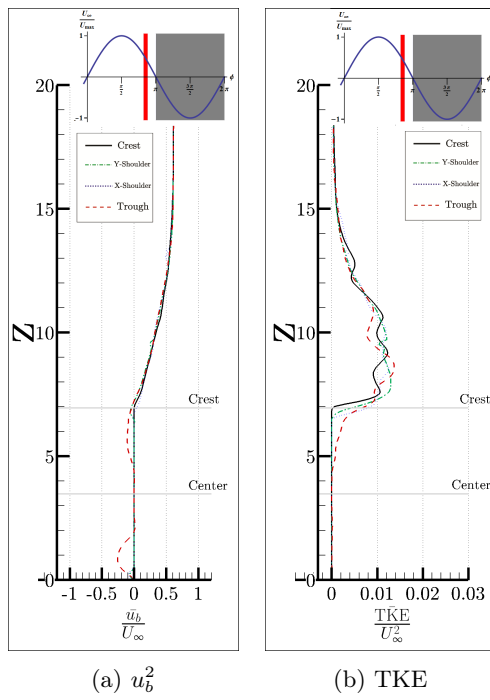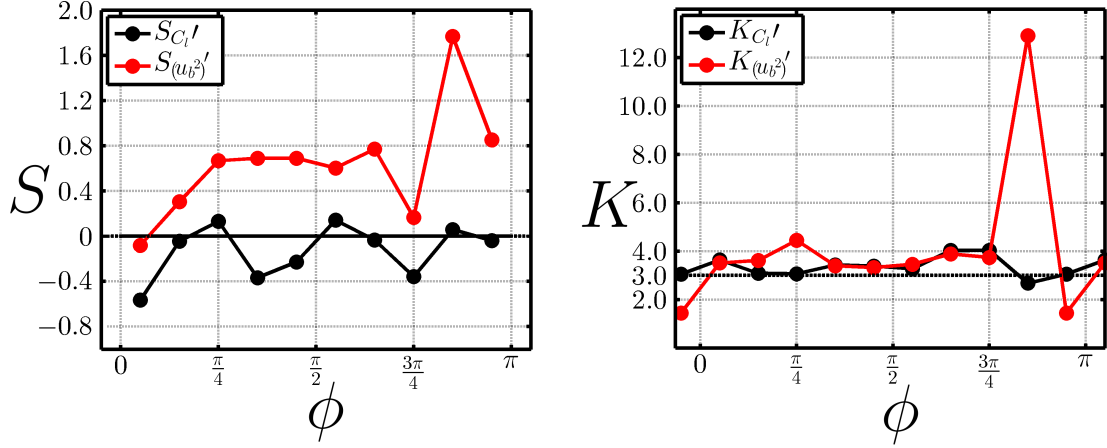(a) u_b^2 (b) TKE

Figure 5.18: The phase-space-averaged u_b and turbulent kinetic energy profile above the sphere crest at $Re_\delta = 200$ at $\phi = \frac{17\pi}{20}$, the phase of the highly peaky PDF of $u_b^{2'}$ in figure 5.15i.
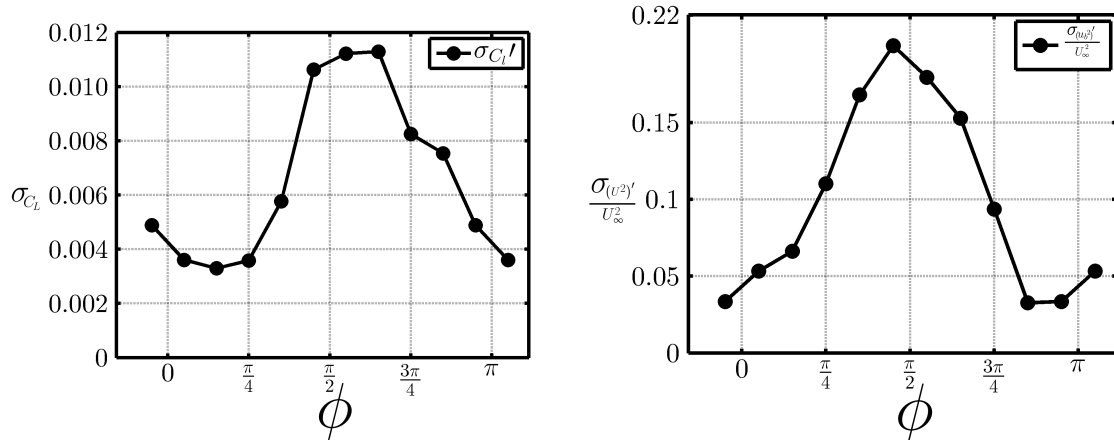
(a) Skewness of the $C_L{}'$ and $u_b^{2'}$ PDFs vs phase in radians.

(b) Kurtosis of the $C_L{}'$ and $u_b^{2'}$ PDFs vs phase in radians.

Figure 5.19: Skewness and Kurtosis of PDFs of lift coefficient, $C_L{}'$, and bed velocity squared, $u_b^{2'}$ at $Re_\delta = 200$. These appear to follow $u_\infty(\phi)^2$.

turbulence properties. The turbulent disturbences leaking from the bed flow above may serve to quickly stimulate flow conditions resembling steady flow. Future studies should aim to characterize the transition of turbulence in the pore space and its potential effect on lift as well as the phase lag of this portion of the flow.

5.5   Future Simulations and Analysis

The new solver will soon be used to simulated larger arrays of particles, and, eventually, their suspension, collision, transport, and deposition. It will also be used to parameterize probability distribution functions of bed velocity intensity and particle lift and drag as a function of phase, and the local flow properties $\frac{D}{L_u}$ and $\frac{\sigma_{u_b}}{\bar{u}_b}$. In order to test the proposed PDF dependencies, and extra layer of spheres will need to be stacked atop the existing one so the pore space turbulence and the influence on the forces experienced by the sediment may be observed. Many more spheres will need to be added so that the statistics of the particle forces and, eventually, motions, will be significant. This will serve the secondary purpose of widening the domain and addressing the issue encountered in the present simulations in which statistics were more strongly correlated from sphere to sphere than from cycle to cycle. Such large simulations might involve hundreds of millions even 1 or 2 billion cells and will be made possible by the new structured solver, which is expected to

(a) Standard deviation of the C_L' PDF vs phase in radians.

(b) Standard deviation of the $u_b^{2'}$ PDF vs phase in radians.

Figure 5.20: Standard deviation of PDFs of the lift force, C_L', and the bed velocity squared, $u_b^{2'}$ at $Re_\delta = 200$.

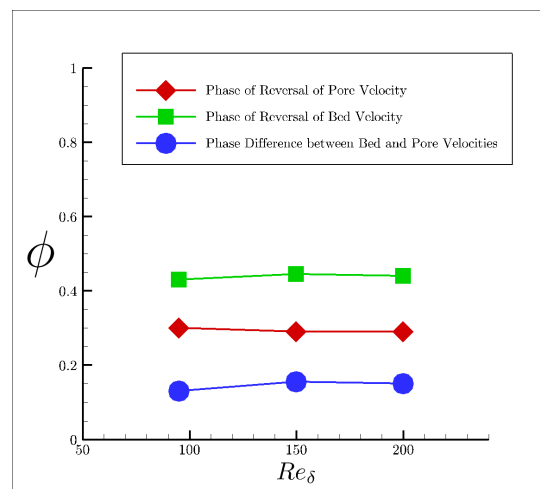Figure 5.21: Phase lag of flow reversal between the bed and pore velocities as a function of Re_δ. Flow reversal in the pore space was computed by averaging $\bar{u}$ over the lower portion of a vertical line-probe tangent to the spanwise extrema of a sphere and observing a change of signs in this value. The same technique was used in the region of $7.05 < \frac{z}{\delta} < 8.05$ for bed-velocity reversal.

increase the size of problems which can be addressed per processor by a factor of 10 to 50 while only decreasing runtime marginally once new pressure solving options are implemented.

Careful temporal flow-force correlations as a function of fluid position will be conducted to visualize which regions have the greatest impact on the flow and ensure more accurate sampling of the bed-flow velocity. This will be accomplished via post processing of the flow-field directly in Fortran, a necessary step for the computational difficulty of running spatially dependent temporal correlations and utilizing large sets of data. The additional option of running spatial filters on the bed velocity will have to be weighed against the practical use of such a filtered velocity; such information is unlikely to be available to large sediment-transport models. The bed-flow velocity can then be sampled and fit with log-normal, Gaussian, and χ^2 distributions. The quality of the fits can then be compared with the parameters of interest as described in section 2.1: $\frac{D}{\delta}$ and $\frac{\sigma_{u_b}}{\bar{u_b}}$. It is the ultimate aim of this effort to find a generalized PDF model which can be integrated to give the instantaneous sediment load supported by the flow, which is expected to vary throughout the cycle. Once an instantaneous model is achieved, the effects of transience can be built upon this.

Chapter 6   Conclusions and Future Work

A new incompressible-flow, finite-volume solver was developed. This was designed to be suitable for use with fully resolved sediment-laden flows. This solver was shown to perform accurately on problems of $\mathcal{O}(10^6)$ cells per processor. It was also validated with periodic, wall, moving wall, and slip boundary conditions on a Taylor-Green vortex and a lid-driven cavity. It was shown to be second-order accurate in space on the Taylor-Green vortex case. A turbulent channel flow was run to validate the solver with turbulent flows. Despite errors of order of 1%, the general trends of the solution were in agreement with a benchmark case [31].

A rigid-body solver, an immersed-boundary method known as the fictitious domain method, was also implemented to simulate sediment particles in the incompressible fluid by imposing fluid rigidity within the particle volume. A grid-refinement study on a confined cylinder subjected to channel flow showed the rigid-body solver to be spatially second-order accurate in the vicinity of the rigid-body interface. The rigid-body solver was validated on cylinders in open flows at $Re = 40$, 100, 300, and 1000.

Fully resolved simulations of oscillatory flow over a single layer of hexagonally packed spheres were run at $Re_\delta = 95$, 150, and 200, the intent being the acquisition of insight leading to improved sediment transport models for coastal environments. The $Re_\delta = 95$ and $\frac{D}{\delta} = 6.95$ case shed light on recent simulations ([16, 22]) due to its improved geometry, which includes pore space and contact points between the spheres. The present characterization of fluid-frame peak velocities above the sphere crests (figure 5.2) appeared to be a better fit of the original experiment than the recent studies of [16, 22]. This case was shown to be fully laminar, in contrast to the simulation of Fornarelli and Vittori (2009) [22] but in agreement with Keiller and Sleath (1975) [30]. Discrepencies in the form of high-wavenumber oscillations were found between the fluid-frame velocity profiles above the spheres in the present $Re_\delta = 95$ case and #41 of [30] (see figure 5.3a). This may suggest an under-resolved flow or particle interface in the present simulation; however, a number of other possible causes of these discrepancies have been suggested, most notably that the transformation of oscillating fluid cases to an oscillating referencing frame may not produce an accurate approximation of the oscillating plate case when the flow is three dimensional, as with roughness elements. Lift profiles were produced (figure 5.13); an unexplained peak in the lift force was found just after flow reversal at $Re_\delta = 95$, while the relative magnitude of C_L was shown to decrease with respect to $\frac{u_b^2}{U_\infty^2}$ as the Reynolds number increased.

The three cases run were used to observe changes in characteristic flow structures at different Reynolds numbers and their effects on the lift and drag of the spheres. Specifically, the horseshoe vortices prominent at $Re_\delta = 95$ diminish with increasing Re_δ due to their being elongated around the sides of the sediment particles and pulled apart. The flow at $Re_\delta = 150$ still featured semistable vortices with mild flapping and a weaker, less distinct ejection near peak velocities at $\frac{\pi}{2}$, while the $Re_\delta = 200$ case showed at least one complete early ejection and reformation of the structure behind the sphere as well as the development of violent vertical flapping near the peak velocities (see figure 5.5). The line probes of $\bar{u}_b$ at this Reynolds number (figure 5.9b) featured a set of inflections indicating a consistent event across the samples, perhaps the early vortex ejection observed during the accelerating phases of the cycle. This suggests the possibility of a trend of earlier vortex ejections with increasing Re_δ

Asymmetrical velocity profiles were observed immediately before peak velocities as local turbulent kinetic energy was rapidly increasing. The proposed explanation for this is that turbulent kinetic energy is primarily generated due to flow instabilities at particle surfaces and that velocity distributions tend to be skewed down gradients of the turbulent kinetic energy. Likewise, symmetrical, nearly Gaussian distributions of the local streamwise velocity were observed shortly before flow reversal, when turbulent kinetic energy was rapidly dissipating. This should provide a context for when the assumption of Gaussian velocity profiles may be appropriate as the basis for stochastic models of particle forces in oscillatory flows.

The dependence of the relationship between the probability distribution functions of $u_b^{2\prime}$ and $C_L{}'$ on the phase of the cycle was explored. The higher moments of the normalized PDFs did not exhibit general correlations between the two parameters; however, the kurtoses appeared correlated near peak velocities, where relative turbulence intensities are expected to be minimal. It is suggested that the single line probe above the crest of the spheres used in this study to sample the bed velocity was too small a sampling region. The probability distribution functions of $u_b^{2\prime}$ approaching flow reversal above the sphere crests exhibited strongly peaked and skewed distributions due to their high relative turbulence intensity; this is unlikely to be exhibited by the whole of the body of turbulent fluid surrounding the spheres, thus the sampling of one specific point line probe for the bed velocity appears to periodically display overly extreme higher moments of the PDFs compared to those of $C_L{}'$. It is also suggested further discrepancies may be due to a lack of high-wavenumber filtering in the bed velocity sampling, which would occur naturally in the integration of dynamic pressure forces acting on the surface of the rigid sediment. The phase difference of flow reversal between the bed velocity and pore velocity across Reynolds numbers was considered and no substantial differences were found, yet it should be noted that turbulence did not develop in the pore space.

Bibliography

[1] Sourabh V. Apte and Justin Finn. A variable-density fictitious domain method for particulate flows with broad range of particle-fluid density ratios. *Journal of Computational Physics*, accepted for publication, 2012.

[2] Sourabh V. Apte, Mathieu Martin, and Neelesh A. Patankar. A numerical method for fully resolved simulation (frs) of rigid particle-flow interactions in complex flows. *Journal of Computational Physics*, 228(8):2712–2738, 2009.

[3] Jim Best, Sean Bennet, John Bridge, and Mike Leeder. Turbulence modulation and particle velocities over flat sand beds at low transport rates. *Journal of Hydraulic Engineering*, 123(12):1118–1129, 1997.

[4] O. Botella and R. Peyret. Benchmark spectral results on the lid-driven cavity flow. *Computers & Fluids*, 27(4):421–433, 1998.

[5] Joseph Calantoni and Christopher S. Thaxton. Simple power law for transport ratio with bimodal distributions. *Journal of Geophysical Research*, 113, 2008.

[6] S. Carstensen, B. M. Sumer, and J. Fredsøe. A note on turbulent spots over a rough bed in wave boundary layers. *Physics of Fluids*, 24, 2012.

[7] Ahmet O. Celik, Panayiotis Diplas, Clinton L. Dancey, and Manousos Valyrakis. Impulse and particle dislodgement under turbulent flow conditions. *Physics of Fluids*, 22, 2010.

[8] Clemens Chan-Braun, Manuel García-Villalba, and Markus Uhlmann. Direct numerical simulation of rough wall open channel flow. Technical report, Proceedings of the 7th International Symposium on Turbulent Shear Flow Phenomena, 2011.

[9] Clemens Chan-Braun, Manuel Garcia-Villalba, and Markus Uhlmann. Force and torque acting on particles in a transitionally rough open-channel flow. *Journal of Fluid Mechanics*, 684:441–474, 2011.

[10] Nian-Sheng Cheng. Influence of shear stress fluctuation on bed particle mobility. *Physics of Fluids*, 18(9), 2006.

[11] Nian-Sheng Cheng and Yee-Meng Chiew. Pickup probability for sediment entrainment. *Journal of Hydraulic Engineering*, 124:232–235, 1998.

[12] Nian-Sheng Cheng and Adrian Wing-Keung Law. Fluctuations of turbulent bed shear stress. *Journal of Engineering Mechanics*, 129:126–130, 2003.

[13] Paola Costamagna, Giovanna Vittori, and Paolo Blondeaux. Coherent structures in oscillatory boundary layers. *Journal of Fluid Mechanics*, 474:1–33, 2003.

[14] Brian W. Dade, Andrew J. Hogg, and Bernard P. Boudreau. *Physics of Flow above the Sediment-Water Interface.* Oxford Unversity Press, 2001.

[15] Martin Detert, Volker Weitbrecht, and Gerhard H. Jirka. Laboratory measurements on turbulent pressure fluctuations in and above gravel beds. *Journal of Hydraulic Engineering*, 136(10):779–789, 2010.

[16] Lei Ding and Qing-He Zhang. Lattice boltzmann simulation to characterize roughness effects of oscillatory boundary layer flow over a rough bed. *Proceedings of the International Conference on Coastal Engineering*, (32), 2010.

[17] Panayiotis Diplas, Clint L. Dancey, Ahmet O. Celik, Manousos Valyrakis, Krista Greer, and Tanju Akar. The role of impulse on the initiation of particle movement under turbulent flow conditions. *Science*, 322:717–720, 2008.

[18] Hans Albert Einstein. The bed-load function for sediment transport in open channel flows. Technical Report 1026, United States Department of Agriculture, Washington, D. C., September 1950.

[19] Justin Finn. *A Numerical Study of Inertial Flow Features in Moderate Reynolds Number Flow Through Packed Beds of Spheres.* PhD thesis, School of Mechanical, Industrial, and Manufacturing Engineering, Oregon State University, Corvallis, OR, 2013.

[20] Paul F. Fischer, Gary K. Leaf, and Juan M. Restrepo. Forces on particles in oscillatory boundary layers. *Journal of Fluid Mechanics*, 468:327–347.

[21] Paul F. Fischer, Gary K. Leaf, and Juan M. Restrepo. Influence of torque on the lift and drag of a particle in an oscillatory flow. *Journal of Fluids Engineering*, 130, 2008.

[22] F. Fornarelli and G. Vittori. Oscillatory boundary layer close to a rough wall. *European Journal of Mechanics B: Fluids*, 28:283–295, 2009.

[23] J. Fredsøe and R. Deigaard. *Mechanics of Coastal Sediment Transport.* Elsevier Science, 1994.

[24] Giménez-Curto and Miguel A. Corniero Lera. Oscillating turbulent flow over very rough surfaces. *Journal of Geophysical Research*, 101:20745–20758, 1996.

[25] B. Hofland. *Rock and Roll.* PhD thesis, Delft University of Technology, 2005.

[26] Bas Hofland and Jurjen A. Battjes. Probability density function of instantaneous drag forces and shear stresses on a bed. *Journal of Hydraulic Engineering*, 132(11):1169–1175, 2006.

[27] N. A. Horton and D. Pokrajac. Onset of turbulence in a regular porous medium: An experimental study. *Physics of Fluids*, 21, 2009.

[28] B. L. Jensen, B. M. Sumer, and J. Fredsøe. Turbulent oscillatory boundary layers at high reynolds numbers. *Journal of Fluid Mechanics*, 206:265–297, 1989.

[29] J. Jiménez. Turbulent flow over rough walls. *Annual Review of Fluid Mechanics*, 36:173–196, 2004.

[30] D. C. Keiller and J. F. A. Sleath. Velocity measurements close to a rough plate oscillating in its own plane. *Journal of Fluid Mechanics*, 73:327–347, 1975.

[31] John Kim, Parviz Moin, and Robert Moser. Turbulence statistics in fully developed channel flow at low reynolds number. *Journal of Fluid Mechanics*, 177:133–166, 1987.

[32] R. V. Krstic and H. J. S. Fernando. The nature of rough-wall oscillatory boundary layers. *Journal of Hydraulic Research*, 39(6):655–666, 2001.

[33] T. S. Lundgren. Linearly forced isotropic turbulence. *Annual Research Briefs*, pages 461–473, 2003.

[34] Jianmin Ma and J. J. R. Williams. Implication of horizontal force moments for the threshold of bed entrainment in an open-channel flow. *Journal of Hydro-environment Research*, 3:2–8, 2009.

[35] Costantino Manes, Dubravka Pokrajac, Ian McEwan, and Vladimir Nikora. Turbulence structure of open channel flows over permeable and impermeable beds: A comparative study. *Physics of Fluids*, 21, 2009.

[36] Cristian Marchioli, Maurizio Picciotto, and Alfredo Soldati. *Interaction between Turbulence Structures and Inertial Particles in Boundary Layer: Mechanisms for Particle Transfer and Preferential Distribution.* Courses and Lectures. 2003.

[37] Andreas Mark and Berend G. M. van Wachem. Derivation and validation of a novel implicit second-order accurate immersed boundary method. *Journal of Computational Physics*, 227:6660–6680, 2008.

[38] R. Mittal, H. Dong, M. Bozkurttas, F. M. Najjar, A. Vargas, and A. von Loebbecke. A versatile sharp interface immersed boundary method for incompressible flows with complex boundaries. *Journal of Computational Physics*, 227:4825–4852, 2008.

[39] Hideaki Mouri, Akihiro Hori, and Masanori Takaora. Large-scale lognormal fluctuations in turbulence velocity fields. *Physics of Fluids*, 21, 2009.

[40] C. S. Nichols and D. L. Foster. Observations of bed form evolution with field-scale oscillatory hydrodynamic forcing. *Journal of Geophysical Researchn*, 114, 2009.

[41] A. N. Papanicolaou, P. Diplas, N. Evaggelopoulos, and S. Fotopoulos. Stochastic incipient motion criterion for spheres under various bed packing conditions. *Journal of Hydraulic Engineering*, 128(4):369–380, 2002.

[42] Walter C. Reade and Lance R. Collins. Effect of preferential concentration on turbulent collision rates. *Physics of Fluids*, 12(10):2530–2540, 2000.

[43] Alexandre M. Roma, Charles S. Peskin, and Marsha J. Berger. An adaptive version of the immersed boundary method. *Journal of Computational Physics*, 153:509–534, 1999.

[44] G. N. Rosenthal and J. F. A. Sleath. Measurements of lift in oscillatory flow. *Journal of Fluid Mechanics*, 164:449–467, 1985.

[45] Giovanni Seminara and Paolo Blondeaux. *Perspectives in Morphodynamics.* Springer, 2001.

[46] A. Shields. Anwendung der aehnlichkeitsmechanik und der turblenzforschung auf die eschiebe-bewegung. *Mitteilungen der Preussiischen versuchsanstalt fur wasserbau und schiffhau*, 26, 1936.

[47] Soo Jai Shin, Wei-Xi Huang, and Hyung Jin Sung. Assessment of regularized delta functions and feedback forcing schemes for an immersed boundary method. *International Journal for Numerical Methods in Fluids*, 58:263–286, 2008.

[48] Julian A. Simeonov and Joseph Calantoni. Modeling mechanical contact and lubrication in direct numerical simulations of colliding particles. *International Journal of Multiphase Flow*, 46:38–53, 2012.

[49] K. M. Singh, N. D. Sandham, and J. J. R. Williams. Numerical simulation of flow over a rough bed. *Journal of Hydraulic Engineering*, 133(4):386–398, 2007.

[50] Joseph Skitka and Sourabh Apte. Characterization of oscillatory boundary layer over a closely packed bed of sediment particles. *8th International Conference on Multiphase Flow*, 2013.

[51] J. F. A. Sleath. Turbulent oscillatory flow over rough beds. *Journal of Fluid Mechanics*, 182:369–409, 1986.

[52] John F. A. Sleath. Transition in oscillatory flow over rough beds. *Journal of Waterway, Port, Coastal, and Ocean Engineering*, 114:18–33, 1988.

[53] John F. A. Sleath. Sediment transport by waves and currents. *Journal of Geophysical Research*, 100:10977–10986, 1995.

[54] Sir George Gabriel Stokes. On the effect of the internal friction of fluids on the motion of pendulums. *Transactions of the Cambridge Philosophical Society*, 9, 1850.

[55] A. A. Townsend. *The Structure of Turbulent Shear Flow*. Cambridge Monographs on Mechanics and Applied Mathematics. Cambridge University Press, 1976.

[56] Markus Uhlmann. An immersed boundary method with direct forcing for the simulation of particulate flow. *Journal of Computational Physics*, 209:448–476, 2005.

[57] Manousos Valyrakis, Panayiotis Diplas, and Clint L. Dancey. Entrainment of coarse grains in turbulent flows: An extreme value theory approach. *Water Resources Research*, 47, 2011.

[58] B. C. Van Prooijen and J. C. Winterwerp. A stochastic formulation for erosion of cohesive sediments. *Journal of Geophysical Research*, 115, 2010.

[59] Leo C. van Rijn. Applications of sediment pick-up function. *Journal of Hydraulic Engineering*, 112(9):867–874, 1986.

[60] G. Vittori and R. Verzicco. Direct simulation of transition in an oscillatory boundary layer. *Journal of Fluid Mechanics*, 371:207–232, 1998.